Temperature-salinity distribution in the Northeast Atlantic from ship and Argo vertical casts.

I. Bashmachnikov[1,2], F. Neves[1], Â. Nascimento[1], J. Medeiros[1], I. Ambar[1,2], J. Dias[1,2], X. Carton[3]

[1] *Centro de Oceanografia da Faculdade de Ciências / MARE – Marine and Environmental Sciences Centre, Universidade de Lisboa, Campo Grande, 1749-016, Lisbon, Portugal, e-mail: igorb@fc.ul.pt.*

[2] *Departamento de Engenharia Geográfica, Geofísica e Energia (DEGGE), Faculdade de Ciências, Universidade de Lisboa, Campo Grande, 1749-016 Lisboa, Portugal.*

[3] *Laboratoire de Physique des Océans, UMR 6523, Université de Bretagne Occidentale, 6 avenue Le Gorgeu, 29200 Brest, France.*

Abstract

The present study defines new interpolation functions for hydrological data. These functions are applied to generate climatological maps of temperature-salinity distribution with 25-m depth interval and 30-km space interval (MEDTRANS data-set). The data undergoes a rigorous initial data quality control, having passed several filtering procedures. The gridding is done on neutral density surfaces, which allows better representation of thermohaline fronts for the same gridding radius. The multi-pass Barnes' Optimum Interpolation procedure with spatially variable size of the gridding window is used. The shape of the window accounts for the dominant along-isobath direction of water mass transport over steeply sloping topography. A local ratio of topographic to planetary β-effects is used to define the shape of the window as a function of the relative importance of the topographic influence. The N/f ratio is applied to account for the baroclinic compensation decay of the topographic influence on water mass transport with the distance from the bottom. The gridded fields are available at the web-site of the Center of Oceanography of the University of Lisbon (http://co.fc.ul.pt/en/data).

The obtained MEDTRANS climatology gives more details of the distribution of water characteristics in the Subtropical Northeast Atlantic than other alternative climatologies and is able to reproduce a number of dynamic features described in literature: the

acceleration in the meanders of the Azores current; the cyclonic gyre in the Gulf of Cadiz; the splitting and separation of the Mediterranean Water outflow in two veins near the Gorringe and the Galicia Banks. Seasonal climatologies, computed for the warm (May-October) and cold (November-April) seasons, reveal stronger zonal extension of the upper ocean patterns during the warm season, as compared to the cold one.

1. Introduction

This work presents detailed maps of climatic temperature-salinity distribution of ocean characteristics in the Subtropical Northeast Atlantic (25-45º N and 6-35º W), with special focus on the propagation of the Mediterranean Water (MW).

The Subtropical Northeast Atlantic region is dominated by two nearly zonal flows: the southern branch of the North Atlantic Current (SNAC) that crosses the Mid-Atlantic Ridge (MAR) at 45-48^{o} N (Bower et al., 2002), and the Azores Current (AzC) that crosses the MAR at 34-35^{o} N (Klein and Siedler, 1989; Jia, 2000). The 60-km wide jet-like AzC separates the warm and salty tropical water from the subtropical water and its dynamic and thermohaline signal reaches 1000 m depth or more (Käse and Siedler, 1982; Volkov and Fu, 2010). The SNAC separates the subtropical water from the colder and fresher subpolar water (Read et al., 2010) and extends over 1000 m. Pollard and Pu (1985) also mention the dominance of the eastward mean drift in the upper 200-300 m layer over the Subtropical Atlantic. More recent studies suggest that the drift is separated in several weak meandering southeastwards jets (Paillet and Mercier, 1997).

Near the Iberian and the northwest African coasts, the Portugal Current (PC) and the Canary Current (CC) constitute a system of wide and shallow ocean flows together with coastally trapped upwelling jets (Martins et al., 2002; Perez et al., 2001; Pelegri et al., 2005, Nolasco et al., 2013). Below the coastal jet of the CC, a deeper northward flow, trapped by the African continental slope, transports the Antarctic Intermediate Water (AAIW) as far as the Gulf of Cadiz (Louarn and Morin, 2011). Underneath the PC, the deep poleward flow incorporates the Mediterranean Undercurrent (MUC), which vertically splits into upper and lower cores (Ambar, 1983; Ambar et al., 2008).

Presently there are several global and regional data bases covering the study region. The most known is the World Ocean Atlas 2009 (WOA09), where a minimum radius of the gridding window of 444 km is used and the grid resolution is 1ºx1°.

During this work, the new version of the World Ocean Atlas 2013 (WOA13) has been published. The WOA13 has a radius of the gridding window of 214-321 km and a maximum grid resolution of 0.25ºx0.25°. It shows a significantly improved climatology in the study region as compared to WOA09. At the same time, the gridding procedure with the radius of influence of more than 200 km significantly oversmoothes the frontal zones, especially near the Iberian continental slope, where the spreading of the MW is characterized by very sharp temperature-salinity gradients. In particular, the MUC is 20-80 km wide and cannot be adequately reproduced in WOA13 (details are given in Section 3). In this study the bottom trapped Mediterranean Undercurrent signature is better reproduced due to the reduction of the local radius of influence to 70 km near the Iberian Peninsula. Additionally, stretching of the gridding window along steep topographic slopes, as well as the use of isopycnic mapping, give advantages in representation of frontal boundaries, compared to the isobaric mapping used in WOA. Isobaric mapping is also known to produce artificial temperature-salinity anomalies in the vicinity of frontal zones, which does not happen for isopycnic gridding procedures (Lozier et al., 1994).

Among other climatologies covering the study region, we consider AMA (Roemmich and Gilson, 2009), MIMOC (Schmidtko et al., 2013) and DIVA (Troupin et al., 2010). AMA climatology is based exclusively on ARGO data. The data-set does not allow mapping the MUC along the continental slope of the Iberian Peninsula (a very few ARGO floats there). Therefore, it will not be used for comparison. DIVA climatology has too much noise in climatic fields and it also will not be used for comparison. The MIMOC climatology has 0.5ºx0.5° resolution and is based on isopycnic mapping. We will show below that our results closely correspond to the results of MIMOC in the upper ocean. At the same time, MIMOC has the disadvantage of lower resolution and of the use of sigma surfaces instead of neutral density surfaces. The climatology is also found to produce artifacts in temperature-salinity distributions below 1500 m (see Section 3).

Neutral density surfaces (McDougall, 1987), used inthis study, are a generalisation of the concept of standard σ_n ($n = 0$, 1, 2, etc.) surfaces. The former are parallel to the latter at their reference level. Along a neutral density surface, change of density due to saline contraction is compensated by thermal expansion: $\alpha \nabla_n \theta - \beta \nabla_n S = 0$, where α is the thermal expansion coefficient and β is the saline contraction coefficient (both are

temperature-salinity-pressure-dependent) and the gradient ∇_n is taken along the neutral density surface. Therefore, a particle travelling along a neutral density surface does not experience the effect of the buoyancy force. This is not true for a particle travelling along a σ_n surface (McDougall, 1987).

The methodology of this study (described in Section 2) complements the existing gridding methods (WOA09, WOA13, Schmidtko et al., 2013, Troupin et al., 2010) and the resulting climatic fields provide additional details on temperature-salinity distributions (described in Section 3). The sufficiently large quantity of data and their rather even spatial distribution allow us to base the parameters of the gridding procedure on characteristics of local hydrodynamics. This increases the realism of the derived regional circulation patterns. The present climatology is obtained in the framework of the project MEDTRANS, and will further be referred as MEDTRANS climatology.

2. Materials and methods

Data from the World Ocean Database (WOD) were downloaded from the National Oceanographic Data Center (NODC, http://www.nodc.noaa.gov/): CTD (Conductivity-Temperature-Depth, high vertical resolution of typically 1 m or less) and PFL (Profiling Float, medium vertical resolution of typically 1-10 m, mainly obtained from ARGO profiling float array), OSD (Ocean Station Data, low vertical resolution of typically more than 10 m) from 1950 to 2011.

Bathymetry data, used for conditioning of some data-filters and for gridding procedures, are obtained from ETOPO2 data-set (http://www.ngdc.noaa.gov/mgg/fliers/01mgg04.html).

Within the study region, there are over 54000 profiles (Table 1). The spatial distribution density of CTD (and to less extent of OSD) profiles show a tendency to decrease from the continental margin seawards. The PFL profiles cover the region rather uniformly, but mostly the areas away from the continent and with water depth exceeding 1000 m. A large amount of the OSD data is concentrated along standard sections, as WOCE A03 section (around 36° N), WOCE AR21/A16 sections (around 20° and 25°W), Portugal-Greenland sections, etc. OSD data mostly cover the years 1970-1995 (with maximum number of casts between 1985 and 1990), CTD data –

1985-2000 (with maximum number of casts between 1990 and 1995), while PFL – 2000-2011 (with maximum number of casts after 2005). Therefore, local biases of final climatology may immerge since different parts of the study region are predominantly covered with casts taken in a particular span of years. The climatic maps are constructed under a priory assumption of no strong interannual variations of water properties in the region since 1950. In limited parts of the region some seasonal biases are also possible, but they should not be significant, since the data are rather homogeneously distributed across the seasons in any part of the region.

A quality control procedure was applied to all z-level profiles from NODC data-set, attributing different flags to the data-points according to their quality. The first step consists in screening for major instrument malfunctions or calibration errors. This consists in verifying whether vertical temperature/salinity profiles significantly deviate from the WOA09 climatological profiles interpolated to the observed profiles' positions. Assuming normal distribution of temperature/salinity deviations from climatology at any depth level, a profile is considered to be bad if the whole profile deviates from the climatological mean profile by more than 5 standard-deviations. Mean standard deviations of 0.07 for salinity and 0.35° C for temperature, derived from WOA09 data-set, are used to form the criterion. If only a part of the profile deviates from WOA09 over 5 standard deviations, the profile is considered "dubious" and the data reliability is verified by eye-checking. The expert decision is made based on persistence of the same "dubious" structures in other local profiles. The filter is not applied for the upper 100-m layer and the MW layer (700-1500 m), since extreme natural deflections from WOA09 climatology in those layers significantly exceed the 5 mean standard deviations used as the filtering criterion.

The next step consists in testing the profiles for static stability. In the parts of the profiles where a density inversion exists and exceeds 0.02 kg m^{-3} over less than 200-m depth range, an attempt to correct the inversion by removing spikes in temperature or salinity is made. For all cases we tend to correct first the salinity spikes, since salinity is typically more vulnerable to observational errors, and then, if necessary, the temperature spikes. Whenever the correction leads to an increase of local standard deviation around the spike in either temperature or salinity, the correction is not applied.

The portions of the profiles treated as "bad" are blanked. If a data gap exists only in the temperature or in the salinity profile, and its size does not exceed 200 m, the gap is linearly (low resolution OSD) or polynomially (CTD and PFL) interpolated. In the latter

case the piecewise cubic Hermite polynomial interpolation is used. This interpolation produces a resulting profile differentiable to the second order, which preserves its extremes and does not suffer from overshooting at the places of abrupt variations in the rate of vertical change of a measured property. Whenever the vertical extension of a gap exceeds 200 m no interpolation is performed. Also no extrapolation is performed at the profile edges. All the "good" profiles are reduced to the standard vertical resolution of 25 m.

The results show that 96% of the casts contained at least 50% of good values for both temperature and salinity, and 93% of the casts contained at least 90% of good values (Table 1). For some selected depth levels, distributions of the data-points that have passed the filtering procedure are presented in Fig. 1 (a-c). In the upper 1900-m layer, the data are rather uniformly distributed (Fig. 1a-b), while below 2000 m, the absence of PFL data results in less dense area covered with observations (Fig. 1c-d). This results in a rapid decrease of the amount of valid data below 1900 m over the study region (Fig. 1d). OSD data form maxima of data concentration at the standard oceanographic levels (Fig. 1d).

Mediterranean Water eddies (meddies) form exceptionally pronounced temperature and salinity anomalies in the mid-ocean in the study region, up to 4°C and 1, respectively (Richardson et al., 2000), and intensive sampling of one of such structures adds a strong local bias to the climatic fields. The casts across meddies are detected using Richardson's criterion (Richardson et al., 1991), i.e. a cast is considered to pass through a meddy, when a salinity anomaly of more than 0.2 over at least a 200-m layer is detected in the depth range between 500 and 1500 m. Those casts are eliminated, together with the surrounding profiles, within 50-km spatial and 30-day time ranges, which may be influenced by the meddy cores. The MUC also forms a strong local temperature-salinity anomaly relative to WOA09 climatology, since area of the MUC is not correctly represented in WOA09. To avoid confounding this climatic feature with meddies, the slope region off Iberia with depths less than 2500 m is excluded from this latter filtration. Removing meddy-related bias, we remove less than 4% of the profiles.

Plotting temperature-salinity distributions for different depth levels, we found consistent positive anomalies of temperature and salinity (relative to WOA09 climatic profiles) in OSD profiles along some of XCTD routes, especially noticeable below the 1500-m level. This feature is not observed for CTD or PFL profiles in the same areas and is presumably due to drawbacks in algorithms for estimation of the depth of XCTD

instruments (Levitus et al., 2008). To eliminate the effect, temperature and salinity deviations of the OSD profiles from WOA09 between 1500 and 2000 m are summed in each of the 100x100 km areas. For the normal distribution of the data deviations from climatology we expect the sum of the deviations to be close to zero, at least within the limits $\pm n\,1.96\,{std}/{\sqrt{n}}$, where n is number of data-points and std is the mean standard deviation of temperature/salinity from climatology (see above). For the typical n=30, we exclude OSD casts whenever the sum of the deviations from WOA09 climatology exceeds 1 in salinity or 4°C in temperature.

In addition, consecutive profiles of PFL (Argo floats) are removed when a degradation of the salinity sensors with time is noticed. Sensor degradation is detected whenever the PFL salinity value starts persistently decreasing with time, at some final part of the float trajectory deviating to more than 5 climatic standard deviations (see above) from the climatology (WOA09) and/or from the mean of the surrounding PFL data over the same time period.

The filtered data entered into a gridding procedure. The gridding is done on neutral density surfaces (McDougall, 1987; Jackett and McDougall, 1997). For this study, pressure, temperature and salinity distributions are obtained at 53 neutral density surfaces (G): 25.50, 25.60, 25.80, 26.00, 26.20, 26.40, 26.60, 26.70, 26.80, 26.90, 26.95, 27.00, 27.05, 27.10, 27.15, 27.20, 27.25, 27.30, 27.35, 27.40, 27.45, 27.50, 27.52, 27.54, 27.56, 27.58, 27.60, 27.62, 27.64, 27.66, 27.68, 27.70, 27.72, 27.74, 27.76, 27.78, 27.80, 27.82, 27.84, 27.86, 27.88, 27.90, 27.92, 27.94, 27.96, 27.97, 27.98, 27.99, 28.00, 28.01, 28.02, 28.03, 28.04. The G-surfaces are selected to be fairly uniformly distributed in depth, keeping the mean distance between the surfaces less than 50 m in the upper 1500-m layer, and less than 100 m below. In the upper 100-m layer, water stability is generally low impeding robust computation of neutral density surfaces. In this layer the isopycnal gridding is substituted by isobaric gridding (Gouretski and Kolterman, 2004).

After calculation of the neutral density surfaces, an additional filter is applied. The computed depth of a neutral density surface can change from one cast to another by as much as 50-400 m within short distances of a few dozens of km. This can be due to a jet-like mean current, as well as due to remnant instrumental errors and eddy noise. Azimuthal velocities and their gradients in eddies are typically higher than velocities and velocity gradients in mean currents, therefore, even when the characteristic length

scales of both dynamic structures are the same, eddies generally deflect isopycnical surfaces more strongly than the mean currents. This difference can be used to design a filter.

Removing points with along-isopycnal pressure gradient over some critical value, limits the vertical velocity variation ($\Delta_z V$) across a G-surface: $\frac{\Delta_z V}{\Delta z} = \frac{\mathrm{N}^2}{f}\frac{\partial G}{\partial l}$, where N is the buoyancy frequency, f is the Coriolis parameter, and l is the direction along the G-surface. Taking $\mathrm{N}^2 = 5\times10^{-5}$ s^{-1} and $\frac{\partial G}{\partial l}$ less than 200 m per 200 km, we filter the variations of $\Delta_z V$ that exceed 5 cm s^{-1} per Δz =100 m. This value of $\frac{\partial G}{\partial l}$ is taken as the critical one. For comparison, the current velocity gradients in the AzC are observed to be less than 3 cm s^{-1} per 100 m (Comas-Rodriguez et al., 2011). On the other hand, about 100 km downstream from the Strait of Gibraltar, the vertical velocity gradient of the MUC, at its upper boundary, reach 30 cm s^{-1} per 100 m (Baringer and Price, 1997). Those vertical gradients are observed only within 10-km distance from the Iberian continental slope, and over the desired 30-km grid resolution of our study the mean vertical gradients in the MUC drop to 12 cm s^{-1} per 100 m. To account for those vertical variations, towards the Iberian Peninsula and in the Gulf of Cadiz the $\frac{\partial G}{\partial l}$ criterion is gradually relaxed to $\Delta_z V$ less than 15 cm s^{-1} per 100 m.

The previous analysis (see also Table 1) gives evidence that the CTD and the PFL profiles have, in general, higher quality than the OSD ones. This is a result of generally lower quality of sensors used with the overall lower vertical resolution. Therefore, in the subsequent gridding procedure the OSD profiles enter with the lower weight of 1, while CTD/PFL data enter with the weight of 2.

The maps of water characteristics are gridded to the Mercator projection used by AVISO altimetry (AVISO). In the study region the grid has 0.33°-resolution in latitude and variable resolution (around 0.30°) in longitude. An advantage of this mesh is that it allows straightforward comparison or merging of the dynamic depths obtained from in-situ data with the free-surface topography available from satellites. The same gridding procedure (see below) is applied for isopycnal and isobaric gridding.

Following WOA methodology, we used the Barnes interpolation procedure for gridding scattered observations to a regular mesh (Barnes, 1964). At a grid point ij,

Barnes interpolation value (F_{ij}) is a weighted sum of temperature or salinity values C_s in observational points s situated inside a certain gridding radius. In the original version of the algorithm, the weights are Gaussian functions of distance r_{ijs} between a grid-point ij and a data-point s: $W_{ijs} = e^{-r_{ijs}^2/R^2}$ (Fig. 2a), where R is the e-folding scale (85% of influence of data points are within $r_{ijs} \le R$). The first-guess gridded fields are formed as: $F_{ij}^0 = \sum_{s:|s-ij|<R} W_{ijs} C_s \Big/ \sum_s W_{ijs}$. Then F_{ij}^0 is interpolated to the positions of the original data-points (F_{ijs}^0) and is refined in the iterative procedure $F_{ij}^k = F_{ij}^{k-1} + \sum_{s:|s-ij|<R} W_{ijs}\left(C_s - F_{ijs}^{k-1}\right) \Big/ \sum_s W_{ijs}$. The iterative process increases the steepness of the interface between the no-pass/pass wavelength domains of the filter, i.e. the sharpness of the resulting frontal zones. Thus, the response function of the first-guess gridded field is $D_0 = e^{-(\pi R/\lambda)^2}$, where wavelength λ is the independent variable. The following iterations decrease the range between the fully filtered and fully accepted wavelengths as $D_k = D_0 \sum_{n=1}^{k} (1 - D_0)^{n-1}$ (Barnes, 1964).

A few modifications to the algorithm introduced in this paper are listed below.

Potential vorticity conservation constrains the direction of quasi-geostrophic ocean flows, in particular, by steering them along topography (Pedlosky, 1987). The inclination of a bottom slope, necessary for effective trapping of the flow, depends on the local ratio of planetary to topographic β-effects. In the absence of friction, the depth-integrated flow is non-divergent (geostrophic) when:

$$V\beta/f - \vec{\nabla}\cdot\nabla H/H = 0. \quad (1)$$

Here the β-plane approximation is used ($f = f_0 + \beta y$), ∇H is the bottom slope, H is the mean water depth, $\vec{\nabla}$ is the horizontal velocity vector and V is its meridional component. At the points where the topographic β-effect dominates over the planetary effect, following Schmidtko et al. (2013), we stretch the Gaussian weight function (W_{ijs}) along isobaths. A methodological novelty in this paper is that, using the

expression (1), the algorithm automatically selects the degree to which the topographic β-effect distorts the circular distribution of the isolines of the weight function W (here and further on, indices ijs are omitted):

The resulting weight function is defined as:

$$W = \left[wc\,A_h + (1-c)\right]e^{-\left(r^2/R^2\right)} \qquad (2)$$

The depth dependent function A_h is taken similar to the one used by Schmidtko et al. (2013): $A_h = \max\left(0.5, \left|1 - 0.5\left|\log\frac{H_{ij}}{H_s}\right|\right|\right)$. The function is dependent on water depth variation between the data point (H_s) and the grid point (H_{ij}). The parameter $c = \delta\frac{\nabla H/H}{\beta/f}$ characterizes the relative role of topographic β-effect relative to the planetary β-effect. The possible variations of the parameter are limited to the range from 0 (no influence of bathymetry) to 1 (the maximum influence of bathymetry). The parameter w (see below) accounts for compensation for the detected decrease of the area of the gridding-window over steep topographic slopes. The ETOPO2 bathymetry used is smoothed over the distances of about half of the gridding window radius R (defined below).

Another novelty of the method is that we account for the effect of ocean baroclinicity, i.e. the weakening of bottom slope effect on the circulation with the distance from the topography. The parameter $\delta = \max\left(0, 1 + \frac{h - H_{ij}}{H_m}\right)$, which is a function of the difference between the gridding level h and the water depth in the grid point (H_{ij}), accounts for this effect. The distance from the bottom, where the bottom influence becomes insignificant on ocean circulation, can be roughly estimated from the expression $H_m \sim L\frac{f}{N}$ (Ownes and Hogg, 1980). With the ratio $\frac{N}{f}$~80-90 (derived from WOA09 data-set), characteristic for the upper 2000-m layer, and the spatial scale $L \sim 200$ km, which is close to the typical width of the major ocean currents, we get $H_m = 2200$-2500 m. The latter value is used for computations (Fig. 2b-d).

It is noted that the expression (2) applied over steep topographic slopes strongly reduces the area with high weights (Fig. 2c, with w=1). In the areas of very steep bottom slope (continental margins, banks or seamounts), the resulting mean weight over the gridding window may decrease to as much as 30%, increasing the noise level of the gridded climatology near the topography. Further on, this noise manifests itself in strong divergence of the computed geostrophic flows, for example. To avoid this effect, the parameter $w \le 1$ is introduced as the ratio of the mean weight inside the gridding window (2) with locally computed c, to the mean weight with $c = 0$. Use of this parameter in expression (2) increases the weights within the gridding window, not affecting the mean gridding radius (Fig. 2d).

When friction is taken into account, the right-hand side of equation (1) is not zero, but includes the effect of the atmospheric wind torque, bottom frictional torque and the Joint Effect of Baroclinicity and Bottom Relief (JEBAR) (Kantha and Clayson, 2000). In the ocean, the JEBAR is generally small compared to other terms. The bottom frictional torque is efficient only near topography and its effect on the flow results in a gradual change of the mean depth or/and of the thickness of a bottom trapped flow. The vorticity pumped into the ocean by the wind torque generates Sverdrup circulation, which, in the eastern parts of the ocean, has a meridional component comparable to the zonal one (Pedlosky, 1998). This is confirmed by the current structure in the Subtropical Northeast Atlantic, derived from in-situ observations (Paillet and Mercier, 1997). These considerations suggest that, in the study region, stretching of the weight function in the zonal direction does not give any benefits to the final product. Since the topographic β-effect at the continental slope or the MAR slopes is several orders higher than the planetary β-effect, then for topographic flow steering other effects can be neglected. Therefore, in this study, the shape of the weight function is only a function of bathymetric slopes.

Finally, to define the weight function (2) we need to define the radius R of the gridding window. Two considerations are taken into account. First, water characteristics at every grid point should be obtained by averaging a sufficient amount of observations, in order to reduce the remnant noise due to time inhomogeneity of the original data-set. A criterion of at least 30 observation points is used, as suggested for obtaining a reasonable estimate of the first moments (Emery and Thomson, 1997). Second, R should be large enough for remnant traces of vortices being filtered out by the gridding

procedure. Variation of data density in horizontal and vertical suggests spatially varying R, as defined below.

Fig. 3 shows that in the upper 1900-m layer the radii of windows containing at least 30 points, increase from the average 30-60 km near the Iberian Peninsula to 60-110 km in the western and southern parts of the study region. On average, over the study region the radius in the upper 1900-m layer is 30-50 km. Below 1900 m, due to a drastic decrease of the number of profiles (Figs. 1d and 3c), the window radius changes across the study region from 60-150 km near the Iberian Peninsula to 150-300 km in the western and the southern parts of the study region. On average over the study region, at 2000 m depth R is 100 km and at 2400 m depth is 170 km.

Mesoscale and submesoscale anomalies of water properties are one of the main sources of noise in climatic data. The effect of eddies is partly removed by the filtering procedures described above. At the same time, some remnant eddy noise still affects the temperature-salinity fields. To further reduce this noise we chose the radius of the gridding window considerably exceeding the typical eddy radius (Appendix 1). By this criterion, R should significantly exceed the characteristic eddy radius of 30 km and preferably exceed the maximum eddy radius of 50-100 km. The value of 60-70 km looks to be a reasonable compromise between the urge towards the desired spatial resolution and the maximum reduction of the mesoscale noise level.

Combining the information above (Figs. 3 and A1), we see that in the upper 1900-m layer in the eastern part of the study region, R is limited by eddy size, while over the rest of the region it is limited by data density. From 2000-m level down R should be doubled, everywhere limited by the data density.

To get the highest possible resolution with the decreasing data density away from the Iberian Peninsula, we used spatially varying R. For G less or equal to 27.96 kg m^{-3} (in the upper 1900-m layer), R is set to 70 km near the Iberian Peninsula and to 200 km in the open ocean. Both radii increase 1.5 times for G from 27.97 to 27.98 kg m^{-3} (in the layer 1900 to 2000 m) and double for G more or equal to 27.99 kg m^{-3} (below 2000 m). A smooth transition between the areas with the minimum and the maximum radii is assured by gradual variation of R across the study region (Fig. 4a-b). In Fig. 3d the Barnes' response functions, after the 3rd iteration, are presented for different R.

Therefore, in the deep ocean the data-set does not permit to perform gridding with higher resolution than that of WOA13, while for the layer above an improvement can be achieved.

For neutral density surfaces the artificial cabelling effect, which results from the spatial averaging during gridding, is tested. These errors are so small that nudging the temperature and salinity values to return to the referred density, as applied by Schmidtko et al. (2013), is not necessary.

Finally, in every grid point, the vertical profiles of temperature and salinity are vertically interpolated into fixed depth levels with 25-m intervals using piecewise cubic Hermite polynomial interpolation. Depths of isopycnals vary across the region, and the chosen set of isopycnals permits the ful coverage the study region down to 2300 m depth.

3. Results

Zonal and meridional sections of temperature and salinity obtained in this paper are presented in Fig. 5. The figure shows that the neutral density surfaces have a rather uniform vertical distribution. Meridional sections of temperature (Fig. 5a-b) show a rapid rise of the isopycnals around 35 °N (the AzC), which is observed down to 1700 m. Farther north, a gradual rise of the isopycnals in the upper 500-m layer corresponds to the dominating eastward flow. In Fig. 5 (a and d), one can also observe the isopycnals bending down near the MAR. This should be due to the MAR being a guide for the southward flows along its eastern slope (Bower et al., 2002).

The MW tongue extends from the Iberian Peninsula to the MAR (Fig. 5d). In the vertical, the influence of the MW extends to at least 2000 m (Reid, 1978; Harvey, 1982; Daniault et al., 1994). The colder water plume at the eastern slope of the MAR below 1500 m corresponds to the Labrador Sea Water (LSW) southward penetration into the eastern subtropical Atlantic (Bower et al., 2002). In the southern part of the region, at 31° N (Fig. 5c), the lower fraction of the MW has the maximum near the African coast between 1000 and 1500 m. The less saline and colder core of the Antarctic Intermediate Water (AAIW) dominates the thermohaline structure along the African coast at around 26-27 °N (Louarn and Morin, 2011).

3.1 Comparison of MEDTRANS annual climatologies with WOA and MIMOC

In this section, the temperature-salinity fields of MEDTRANS climatology, obtained in this paper, are compared to other existing annual climatologies: WOA09, WOA13 and MIMOC (Figs. 7-9).

Fig. 7 shows that temperature differences between the climatologies at 600 m do not exceed 1°C. It is seen that the differences relative to WOA09 data-set are organized in zonally extended patterns (Fig. 7 a, b and c). The areas of higher temperature at 600 m (Fig. 7f) correspond to the positions of the zonal jets – the branches of the NAC at 40° and 45° N (Maximenko et al., 2008). These zonal jets are seen in MIMOC, but the distribution of the characteristics in the open ocean and coastal zones in MIMOC are oversmoothed as compared to MEDTRANS (Fig. 7 a and e, d and g). MEDTRANS climatology also shows a much sharper frontal zone of the AzC than MIMOC or WOA09 climatologies. Fewer differences are observed with WOA13. Compared to WOA13, MEDTRANS climatology presents more details of the upper MW core spreading along the Iberian Peninsula, especially at its southern coast and at the Galicia Bank (Fig. 7 d, h and i).

Fig. 8 presents the salinity distribution at 1200 m, the typical depth of the lower MW core. The differences between the climatologies do not exceed 0.1. MEDTRANS climatology brings significantly more details on the shape of the MW tongue than WOA09 or MIMOC (Fig. 8, a-g). In particular, zonally extended MW maximum between 30º and 33°N, from the Madeira archipelago to Cruiser-Great Meteor seamounts (30-33° N), is seen with higher detail in MEDTRANS. MEDTRANS climatology also makes noticeable a weaker tongue which encounters the Azores plateau from the south at 35-36° N (Fig. 8a). Compared to other climatologies, MEDTRANS climatology reproduces in much more detail two intrusions of the Subarctic Intermediate Water (SIAW) and the LSW (Arhan, 1990; Bower et al., 2002): along the northeastern part of the Azores plateau (37-40°N, 24-28°W) and along the Kings rise/trough (42-45°N and 21-25°W). At the Iberian Peninsula, the important additional details of MEDTRANS climatology is the MUC separation into 2 branches at the southern slope of the Galicia Bank (Fig. 8 d, h and f). Those details are missing in all climatologies, including WOA13.

At 1700 m (Fig. 9a-c), MEDTRANS climatology presents more details in the structure of the deeper portion of the MW tongue as compared to WOA09, but is not intrinsically different from WOA13 (Fig. 9g-i). At the same time, MIMOC climatology

shows a strange finger-like MW salinity pattern between 35º and 43°N (Fig. 9e-f). Salinity profiles of MIMOC climatology (Fig. 9d, profiles 3) show unrealistically deep MW influence, which cannot be identified in the original data distributions at those deep levels (Figs. 1b and 9d). The same feature is observed in temperature (not shown). This is an artefact of MIMOC climatology.

Spatial distributions for a layer mean N^2 are generally similar for all the three data-sets (Fig. 10). For the same latitude, N^2 is a proxy for potential vorticity and its distribution can be used for detection of water masses. N^2 distribution in the upper main thermocline (Fig. 10, a-c) displays lower values in the northeastern corner, corresponding to the areas of generation and spreading of the polar fraction of the East Atlantic Central Water (Pollard et al., 1996; Paillet and Mercier, 1997). At intermediate water levels (Fig. 10, d-f), a N^2 minimum is situated at the Iberian Peninsula and is a sign of the MW. Another minimum, extending along the African coast from 25 to 33° N, corresponds to the AAIW northward penetration (Louarn and Morin, 2011). At deep water levels (Fig. 10, g-h), the N^2 minimum in the northwestern corner of the region, extending southeast along the eastern slope of the MAR is due to the southward spreading of the LSW (Bower et al., 2002). At those levels, MIMOC again shows artificial structures in N^2, compared to other climatologies. Anomalously low N^2 at those levels in MIMOC results from anomalously weak vertical variations of temperature and salinity at deep levels of this area (Fig. 9d, point 3).

Fig. 11 shows geostrophic currents referred to the 1900-m level, computed from the MEDTRANS, WOA13 and MIMOC annual climatologies. Currents from WOA09 climatology are not presented since they are too much over-smoothed even compared to MIMOC climatology. The 1900-m depth is chosen as the reference level, since the adjacent layers present the smallest variations of isopycnal depth over the study region. The reference-level currents in the study region, derived from Argo floats, are of order of 1 cm s^{-1} (Calheiros and Bashmachnikov, personal communication), which can be taken as the measure of the computational error of the upper ocean current velocities.

Fig. 11 (a) shows the currents at 100 m depth, while Fig. 11 (b) displays the mean currents derived from AVISO altimetry (AVISO). The AVISO currents are averaged from 1992 to 2012. The latest version of the mean dynamic topography CNES-CLS09_v1.1 (Rio et al., 2011) is used for computation of the current velocities.

The MEDTRANS currents are similar in structure and speed to those obtained from altimetry. MEDTRANS climatology shows the same velocities for the AzC as in AVISO, although the flow in MEDTRANS is a bit too wide. MEDTRANS climatology also shows intensifications of the flows in the northern and southern parts of the Gulf of Cadiz, as well as south of the Canary Islands. It also reproduces an anticyclonic re-circulation south of AzC at 31-35° W and a cyclonic circulation if the Gulf of Cadiz at 9-10° W, as well as merging of the two branches of the SNAC west of the MAR: one enters the study region at 40°N and the other at 44°N.

The comparison with MIMOC climatology, clearly shows advantages of MEDTRANS results in detailed representation of the circulation patterns (Fig.11d). There are more similarities with the geostrophic currents estimated from WOA13 (Fig.11c). Still, the latter gives less evidence of the AzC meandering and periodic intensification, observed in AVISO and MEDTRANS maps. Also WOA13 climatology does not reproduce the cyclonic gyre in the Gulf of Cadiz (Fig. 11a-b), as well as the MUC (Fig. 11e-f) along the northern slope of the Gorringe Bank and the southern slope of the Galicia Bank (Iorga and Losier, 1999).

Fig. 11 (a) shows that the AzC decelerates as it turns north in quasi-stationary meanders and accelerates as it turns south. This feature is also registered in AVISO results (Fig. 11b), but is absent in WOA13 results (Fig. 11c). The strongest stationary meander is situated at 21-22° W (in AVISO data – at 23° W) and the second one at 16-17° W (the same in AVISO data). Farther on (Section 3.2), we will show that the meander at around 21-22° W is mostly pronounced during winter and nearly disappears in summer (Fig. 13a-b). The same type of seasonal variations is also observed in AVISO altimetry currents (not shown).

The observed deceleration in the AzC in the meanders, as the jet turns north, is accompanied by widening of the jet and an outflow from the jet to the north at 22 and 17° W (Fig. 11a). The merging of the streamlines and the acceleration of the AzC, as the jet turns south, is accompanied by inflows into the AzC from the north at 20, 16 and 13° W. The southward meandering of the AzC ends with the branches to the south at 17 and 12°W (there are also outflows at 31-32 and 27-28° W). Therefore quasi-stationary meanders in the AzC form semi closed water circulations to the north and to the south of the jet. Those features are missing in WOA13 or MIMOC climatologies. The abovementioned inflows/outflows to/from the AzC jet, as it meanders, may be a result

of the accumulated effect of cross-jet migrations of particles subjected to inertial forces (Cushman-Rosin, 2010). At the same time, estimated local inertial effects are small, within 1% of the computed geostrophic current velocities, and do not affect the presented flow structure.

The symmetry of the water inflows/outflows in a meandering current, predicted by the theory, is broken in nature by the vorticity constraint. The anticyclonic vorticity pumped into the ocean by the wind demands the overall flow to go south (the Sverdrup flux). Therefore, the currents are more readily merging the AzC from the north and leaving it to the south, than vice versa.

3.2 Seasonal variability in MEDTRANS climatology

The gridding procedure is repeated for the warm (May to October) and the cold (November to April) seasons. The data are nearly equally distributed over the year: the cold season contains 25000 profiles, while the warm one contains 29000 profiles. The mean window size containing at least 30 points increases by 30-50% (depending on the G-level and the season), as compared to that derived from the complete data-set (Fig. 3a-c). Therefore, to keep the distributions smooth enough, we increase the Barnes gridding radius by 50%: relative to the annual climatic mean (Section 3.1). Thus, for G less or equal to 27.96 kg m^{-3} (the upper 1900-m layer), R is taken 150 km near the Iberian coast and 300 km in the western side of the region. Its spatial variation is similar to the one presented in Fig. 4 (a).

Fig. 12 presents salinity distributions during the cold (Fig. 12 a, d and g) and warm (Fig. 12 b, e and h) seasons at selected water levels, as well as the respective differences between the seasons (Fig. 12 c, f and j). In the upper thermocline (Fig. 12a-c), the cold season is characterized by a hump-like feature between 15 and 25° W at around 35° N, while in summer the isohalines are closer to zonal. The effect is clearly seen in the seasonal change in the intensity of the AzC meander in this region (Fig. 13a-b). This seasonal pattern has been first described by Käse and Siedler (1982). The feature is not seen in WOA13 seasonal climatologies of salinity and geostrophic currents, but is well reproduced in the corresponding MIMOC seasonal climatologies (not shown). More strict zonal extension of the flows in summer can be explained by the seasonal difference in the wind induced ocean vorticity. In summer, winds are weaker in the study region (except for the trade winds in the Canary upwelling area). The resulting

seasonal weakening of the wind stress curl by 50% (Dee et al., 2011) leads to reduction of the meridional Sverdrup transport. Therefore, equation (1) is satisfied better than during the cold season, and currents tend to become more closely aligned with the contours of constant f (when their directions are not conditioned by steep topographic slopes).

Along the western coast of the Iberian Peninsula and the northwestern coast of Africa (from the Canary islands to the Gulf of Cadiz), water at 200 m depth is fresher (Fig. 12c) and colder (not shown) during the warm season, when stronger southward winds along the coast form/intensify the coastal Portugal and Canary upwellings (Navarro-Perez and Barton, 2001; Fraile-Nuez et al. 2010). This feature is well reproduced by both WOA13 and MIMOC seasonal climatologies (not shown). This results in a stronger uplift of the isopycnals along the coasts in summer, registered in zonal sections of MEDTRANS climatology. For example, along the northwestern African coast, the difference changes from a few meters at 34° N (Casablanca) to 25 m between 28° N (the Cape Jubi) and 33° N, and to more than 50 m at 26° N (Cape Bojador). The seasonality in the uplift quickly decreases to a few meters at 250-350 m depth between 28 and 33° N, but is observed down to 600 m at 26° N.

In the intermediate water levels, the spreading of the MW shows little seasonality (Fig. 12d-f). Still, during the warm season the MW salinity tongue at the level of the lower MW core (1000-1300 m) is more squeezed in the meridional direction and stretched further west. In WOA13 and MIMOC seasonal climatologies those seasonal variations are less pronounced (not shown). The observed seasonality may be a result of a change of the intermediate layer circulation as a response to the seasonal intensification in the wind forcing, described above. Northeast of the Canary Islands, along the African coast, the farther northward penetration of the AAIW during spring-summer seasons (Machin and Pelegri, 2009), is also registered in MEDTRANS – a negative salinity anomaly in the warm-cold seasons difference (Fig. 12f). The patterns of geostrophic circulation at intermediate levels are presented for the 700 m depth in Fig. 13 (c-d). The current patterns mostly show the same tendency as in the upper thermocline, being more extended in the zonal direction during summer. In particular, we note a summer intensification of the zonal flow north of the Gorringe Bank. Though the weak currents at those depths may be influenced by non-zero flows at the reference level (of around 1 cm s^{-1}), existence of seasonality in the current patterns is supported

by seasonality in temperature-salinity patterns (Fig. 12d-f). Some very weak traces of those seasonal patterns can be detected in MIMOC seasonal climatology, while WOA13 seasonal climatology does not show any clear circulation patterns at those depths (not shown).

Salinity (and temperature) distributions at 1600 m depth (Fig. 12g-i) suggest that seasonality at those depths is very weak, except for the deeper part of the Iberian continental margin.

Fig. 14 shows depth and intensity of the near-slope salinity maxima along the Iberian coast, i.e. the characteristics of the lower core of the MUC. The results show that, on average, during the warm season the MUC is more saline by 0.02-0.04, and the computed density at the maximum salinity level is larger by 0.01 kg m^{-3}. This may result from a more saline summer outflow from the Mediterranean Sea (Sparnocchia et al., 1994), as well as from higher salinity of the entrained NACW.

The apparent increase of the MEDTRANS gridded salinity along the southern margin of the Iberian Peninsula (Fig. 14, 7-8.5° W), results from oversmoothing of the MUC characteristics in the immediate vicinity of the Gibraltar Strait. In this area the MUC is only 20-50 km wide (Baringer and Price, 1997) and the 70-km gridding window produces its artificial mixture with the fresher and colder NACW. At the same time, the depth of the core should be correctly represented in the climatology. Interesting features are sudden changes of the depth of the lower MW core at some topographically relevant locations, otherwise being quite stable. Thus, the depth of the MUC increases by 30 m around the Portimão canyon, then decreases by around 100 m at Cape St. Vincent (37° N, winter) or 1° north of it (summer), at Aveiro canyon (40.5-41° N) and at the Cape Finisterre (43° N). These results are in accordance with previous estimates of along-slope variations of the depth of the MW salinity maximum (Daniault et al., 1994; Bower et al., 2002).

Another feature observed in the climatology is the change of thickness of the salty MW along the Iberian continental slope, represented as vertical segments in Fig. 14. The thickness is computed between isohalines corresponding to 99% of the maximal salinity at the section perpendicular to the isobaths (the same results are obtained using a fixed value of 36.9 for the isohaline). The thickness of the flow increases up to 38-39° N (southern flank of the Estremadura Promontory) and then starts decreasing. The MW outflow from the Straits of Gibraltar entrains ¾ of the volume while passing the first 20-

40 km along the northern slope of the Gulf of Cadiz at the depths of 250-500 m. Farther on, entrainment into the MW continues, but to a lesser degree (Baringer and Price, 1999). The observed tendencies in the MW core thickness near the Iberian Peninsula suggest that the Estremadura Promontory is a boundary between the MUC dominated by entrainment of the surrounding water into it and the MUC dominated by dispersion of the water from it.

4. Conclusions

The MEDTRANS climatology is based on Barnes' optimum interpolation procedure on 53 neutral density surfaces. Due to lower along-surface gradients of temperature and salinity, as compared to the isobaric surfaces, the isoneutral gridding represents better areas of sharp thermal and haline fronts for the same gridding radius. This is further proven when computing geostrophic current velocities in comparison with the existing high-resolution isobaric datasets (WOA09 and WOA13). The hydrological data used for compiling the climatology have undergone a rigorous quality control, having passed several filtering procedures, including filtering on neutral density surfaces. Reducing eddy related and instrumental noise, the filtering allows sufficient smoothness of the final thermohaline fields at the enhanced spatial resolution. The gridding window radius decreases towards northeast allowing to use the most from the high amount of data near the Iberian Peninsula. In particular, this leads to a better representation of thermohaline fronts of the Iberian upwelling and the MUC. The final climatological maps of temperature and salinity distributions are further vertically re-gridded to the isobaric levels to have a 25-m depth interval with around 30-km horizontal resolution.

MEDTRANS gridding procedure can be regarded as a development of some of the ideas used for obtaining MIMOC dataset (Schmidtko et al., 2013). Still there are a few important differences, which allow MEDTRANS dataset to show several advantages as compared to the MIMOC one. Based on vorticity considerations, topographic influence on dominant along-slope direction of water mass propagation at steep slopes is taken into account through the shape of the gridding function. The degree to which the gridding weights are aligned with the isobaths along steep slopes depends on the ratio of topographic to planetary β-effects. Limitations on the maximum possible stretching of the gridding window along isobaths increases reliability of the results along very steep

slopes, where otherwise the weight function elongates in a very thin line with only a few observational points inside. Baroclinic decrease of the topographic effect with the distance between the gridding level and the ocean bottom is taken into account: the maximum distance of the topographic influence is proportional to N/f ratio. In the study region the ratio is taken constant, as observed. For larger regions a decrease of the ratio towards the equatorial region and its strong increase towards polar waters should be accounted for. For example, in the polar regions the currents are nearly barotropic and the transition occurs in a jump when crossing the subpolar and polar fronts (Cuny et al., 2002; Losch and Schröter, 2004);.

We did not stretch the weight function in the zonal direction, whenever the influence of the bathymetry can be neglected. This is justified over most of the ocean, where the wind stress curl forces a sensible meridional component of the flow. At the same time, the zonal extension may give advantages near the equator where, due to the strong meridional gradient of the Coriolis parameter, the zonal extension of the flow is well pronounced (Schmidtko et al., 2013).

The MEDTRANS climatology gives more details on the distribution of water characteristics in the upper 2000-m layer over the Subtropical Northeast Atlantic, as compared to other climatologies. As in other climatologies, the meandering together with the seasonal and interannual variations of the current position enlarge the width of the jets in the mean climatic fields as compared to snapshot characteristics of the currents. At the same time, the geostrophic currents, derived from MEDTRANS climatology, reveal several features, not reproduced by the existing climatologies, but in close correspondence with independent observations (e.g. Lozier et al., 1995; New et al., 2001) and with theory (Cushman-Rosin, 2010): (i) periodic intensification of the AzC as it turns south in the quasistationary meanders; (ii) inflows and outflows in the AzC meanders; (iii) recirculation of the AzC west of Cruiser-Great Meteor seamounts; (iv) cyclonic beta-gyre in the Gulf of Cadiz. At 1000 m depth, the geostrophic currents referred to 1900 m level, derived from the MEDTRANS dataset, show two veins of the MUC along the western slope of the Iberian Peninsula: one travels along the slope, while the other separates from the slope around the Gorringe Bank and then merges with the other vein, south of the Galicia Bank. Here the MUC splits again into a vein along the continental slope directed north and along the southwestern slope of the Galicia Bank directed northwest. Those veins have been registered by an independent

analysis (Iorga and Losier, 1999), but do not appear in WOA13 or MIMOC climatologies.

The seasonality of the MW water manifests itself in stronger zonal extension of the patterns during the warm season. This may be related with the decrease of the wind stress curl, and the related meridional Sverdrup transport. Near the Iberian slope, during the warm season it is observed the more saline and denser lower core of the MUC, which is not correctly represented in alternative climatologies, including WOA13.

The gridded temperature-salinity fields are available at the web-site of the Center of Oceanography of the University of Lisbon (http://co.fc.ul.pt/en/data).

Appendix 1

To obtain an indication of the value of R, which filters the remnant eddy noise, decorrelation spatial scales of temperature-salinity data are computed for each data point. Only the points which have at least 10 neighbouring observations within a 200 km radius and a 30-day period are used (Fig. A1). The decorrelation scales are estimated in 3 ways: as the point of zero crossing of a cosinusoidal fit to the autocorrelation function, as the integral of the normalized autocorrelation function – from zero to the first zero-crossing, and as the integral of the square of the normalized autocorrelation function over its definition range (Stammer, 1997).

The histogram of the decorrelation scales, a proxy for eddy radii, (Fig. 4) shows that the scales have two modes: at 10-20 km and around 30 km, and ranging from 10 to 100 km. The latter mode is close to the Rossby radius of deformation in the study region (Emery et al., 1984). The distribution of the decorrelation radii does not show any significant variations across the study region, neither with latitude, nor with the proximity to steep topography. The latter values compare well with the previous studies in the region. In-situ observations suggest eddy radii between 40 and 100 km in the area of the AzC (Gould, 1985; Pollard and Pu, 1985; Pingree and Sinha, 1998; Alves and Verdiere, 1999; Alves et al., 2002; Pingree, 2002; Mourino et al., 2003) and 10 to 60 km in the northern part of the study region (Arhan and Colin de Verdiere, 1985; Mercier and Colin de Verdiere, 1985; Shoosmith et al., 2005), as well as in upwelling area near the Iberian peninsula (Pingree and LeCann, 1992; Oliveira et al., 2004). Derived from the satellite altimetry, the characteristic eddy scales in the study region, are estimated to

be 40-80 km (Le Traon et al., 1990) and 60-100 km (Stammer, 1997; Jacobs et al., 2001; Chelton et al., 2011). The overall larger radii derived from the AVISO altimetry are biased by the cut-off length of 40-50 km, below which eddies cannot be detected with the gridded altimetry data.

Acknowledgments

The authors acknowledge the scientific project MEDTRANS (PTDC/MAR/117265/2010), sponsored by the Portuguese Foundation for Science and Technology (FCT) and the Center of Oceanography of the University of Lisbon (CO-Pest-OE/MAR/UI0199/2011). I.B. also acknowledges the contract C2008-UL-CO-3 of Ciência 2008 between Foundation for Science and Technology (FCT) and the University of Lisbon (UL).

References

Alves, M.L.G.R., and de Verdière, A.C.: Instability dynamics of a subtropical jet and applications to the Azores current system: eddy-driven mean flow, *Journal of Physical Oceanography*, 29**,** 837-864, 1999.

Alves, M.L.G.R., Gaillard, F., Sparrow, M., Knoll, M., and Giraud, S.: Circulation patterns and transport of the Azores front-current system, *Deep-Sea Research II*, 49, 3983-4002, 2002.

Ambar, I.: A shallow core of Mediterranean water off western Portugal, *Deep-Sea Research A*, *30*(6), 677-680, 1983.

Ambar, I., Serra, N., Neves, F., and Ferreira, T.: Observations of the Mediterranean Undercurrent and eddies in the Gulf of Cadiz during 2001, *Journal of Marine Systems*, 71(1), 195-220, 2008.

Arhan, M., and Colin de Verdiere, A.: Dynamics of eddy motions in the eastern North Atlantic, J. Phys. Oceanogr., 15, 153–170, 1985.

Arhan, M.: The North Atlantic Current and Subarctic Intermediate Water, Journal of Marine Research, 48, 109-144, 1990.

AVISO data set. The altimeter products were produced by Ssalto/Duacs and distributed by Aviso, with support from Cnes. WWW page, http://las.aviso.oceanobs.com/las/servlets/dataset.

Baringer, M.N., and Price, J.F.: Mixing and Spreading of the Mediterranean Outflow, J. Phys. Oceanogr., 27, 1654–1677, 1997.

Baringer M.N., and Price, J.F.: A review of the physical oceanography of the Mediterranean outflow. Marine Geology, 155(1), 63-82, 1999.

Barnes, S.L.: A Technique for Maximizing Details in Numerical Weather Map Analysis, Journal of Applied Meteorology, 3, 396–409, 1964.

Bower, A.S., Le Cann, H., Rossby, T., Zenk, W., Gould, J., Speer K., Richardson, P.L., Prater, M.D., and Zhang, H.M.: Directly measured mid-depth circulation in the North Atlantic Ocean, Nature, 419, 603-607, 2002.

Chelton, D.B., Schlax, M.G., and Samelson, R.M.: Global observations of nonlinear mesoscale eddies, Progress in Oceanography, 91, 167-216, 2011.

Cipollini, P., Cromwell, D., Jones, M.S., Quartly, G.D., and Challenor, P.G.: Concurrent altimeter and infrared observations of Rossby wave propagation near 34^{o}N in the Northeast Atlantic, *Geophysical Research Letters*, 24 (8), 889-892, 1997.

Comas-Rodríguez, I., Hernández-Guerra, A., Fraile-Nuez, E., Martínez-Marrero, A., Benítez-Barrios, V.M., Pérez-Hernández, M.D., and Vélez-Belchí, P.: The Azores Current System from a meridional section at 24.5°W, J. Geophys. Res., 116, C09021, doi:10.1029/2011JC007129, 2011.

Cuny, J., Rhines, P.B., Niiler, P.P., and Bacon, S.: Labrador Sea boundary currents and the fate of the Irminger Sea Water, *Journal of Physical Oceanography*, *32*(2), 627-647, 2002.

Cushman-Roisin, B.: Environmental Fluid Mechanics, John Wiley & Sons, NY, pp.400, 2010.

Daniault, N., Mazé, J.P. and Arhan M.: Circulation and mixing of Mediterranean Water west of the Iberian Peninsula, Deep-Sea Research I, 41 (11/12), 1685-1714, 1994.

Dee, D.P., Uppala, S.M., Simmons, A.J., Berrisford, P., Poli, P., Kobayashi, S., Andrae, U., Balmaseda, M.A., Balsamo, G., Bauer, P., Bechtold, P., Beljaars, A.C.M., van de Berg, L., Bidlot, J., Bormann, N., Delsol, C., Dragani, R., Fuentes, M., Geer,

A.J., Haimberger, L., Healy, S.B., Hersbach, H., Hólm, E.V., Isaksen, L., Kållberg, P., Köhler, M., Matricardi, M., McNally, A.P., Monge-Sanz, B.M., Morcrette, J.J., Park, B.K., Peubey, C., de Rosnay, P., Tavolato, C., Thépaut, J.N. and Vitart, F.: The ERA-Interim reanalysis: configuration and performance of the data assimilation system, Q.J.R. Meteorol. Soc., 137, 553–597, doi: 10.1002/qj.828, 2011.

Emery, W.J., Lee W.G. and Magaard L.: Geographic and Seasonal Distributions of Brunt–Väisälä Frequency and Rossby Radii in the North Pacific and North Atlantic, J. Phys. Oceanogr., 14, 294–317, 1984.

Emery, W.J., Thomson, R.E.: Data analysis methods in physical oceanography, Pergamon, UK, pp.1-634, 1997.

Fraile-Nuez, E., Machín F., Vélez-Belchí P., López-Laatzen F., Borges R., Benítez-Barrios V. and Hernández-Guerra A.: Nine years of mass transport data in the eastern boundary of the North Atlantic Subtropical Gyre, J. Geophys. Res., 115, C09009, doi:10.1029/2010JC006161, 2010.

Gouretski, V.V. and Koltermann, K.P.: Berichte des Bundesamtes für Seeschifffahrt und Hydrographie Nr. 35, 2004.

Gould, W.J.: Physical oceanography of the Azores front, *Progress in Oceanography*, 14, 167-190, 1985.

Harvey, J.: θ-S relationships and water masses in the eastern North Atlantic, Deep-Sea Research, 29 (8A), 1021-1033, 1982.

Jacobs, G.A., Barron, C.N., and Rhodes, R.C.: Mesoscale characteristics, J. Geophys. Res., 106, 19581–19595, 2001.

Jackett, D.R., and McDougall, T.J.: A Neutral Density Variable for the World's Oceans, *J. Phys. Oceanogr.*, **27**, 237–263, 1997.

Jia, Y.: Formation of an Azores Current Due to Mediterranean Overflow in a Modeling Study of the North Atlantic, Journal of Physical Oceanography, 30, 2342-2358, 2000.

Iorga, M.C., and Lozier, M.S.: Signature of the Mediterranean outflow from a North Atlantic climatology: 1. Salinity and density fields, Journal of Geophysical Research, 104 (C11), 25985-26009, 1999.

Kantha, L.H., and Clayson, C.A.: Numerical models of oceans and oceanic processes. International Geophysics series v.66, Acad. Press, San Diego, 1-887, 2000.

Kase, R.H., and Siedler, G.: Meandering of the subtropical front south-east of the Azores, *Nature*, 300 (5889), 245-246, 1982.

Klein, B. and Siedler, G.: On the origin of the Azores current, *Journal of Geophysical* Reseach, 94(C5), 6159-6168, 1989.

Le Traon, P.Y., Rouquet, M.C., and Boissier, C.: Spatial scales of mesoscale variability in the North Atlantic as deduced from Geosat data, J. Geophys. Res., 95 (C11), 20267-20285, 1990.

Levitus, S., Antonov, J., Boyer, T.: Global ocean heat content 1955-2007 in light of recently revealed instrumentation problems, Geophys. Res. Lett., 36, L07608, doi:10.1029/2008GL037155, 2008.

Losch, M., and Schröter, J.: Estimating the circulation from hydrography and satellite altimetry in the Southern Ocean: limitations imposed by the current geoid models, *Deep Sea Research I*, *51*(9), 1131-1143, 2004.

Louarn, E., and Morin, P.: Antarctic Intermediate Water influence on Mediterranean Sea Water outflow, Deep Sea Research I, 58 (9), 932-942, 2011.

Lozier, M.S., McCartney, M.S., and Owens, W.B.: Anomalous anomalies in averaged hydrographic data, *Journal of Physical Oceanography*, *24*(12), 2624-2638, 1994.

Lozier, M.S., Owens, W.B., and Curry, R.G.: The climatology of the North Atlantic, Progress in Oceanography, 36 (1), 1-44, 1995.

Machín, F., and Pelegrí, J.L.: Northward Penetration of Antarctic Intermediate Water off Northwest Africa, J. Phys. Oceanogr., 39, 512–535, 2009.

Martins, C.S., Hamann, M., Fuiza A.F.G.: Surface circulation in the eastern North Atlantic from drifters and altimetry, Journal of Geophysical Research, 107, 3217, 2002.

Maximenko, N.A., Melnichenko, O.V., Niiler, P.P., and Sasaki, H.: Stationary mesoscale jet-like features in the ocean, Geophysical Research Letters, 35(8), 2008.

McDougall, T.J.: Neutral density surfaces, J. Phys. Oceanogr., 17, 1950–1964, 1987.

Melet, A., Nikurashin, M., Muller, C., Falahat, S., Nycander, J., Timko, P.G., Arbic, B.K. and Goff., J.A.: Internal tide generation by abyssal hills using analytical theory, J. Geophys. Res. Oceans, 118, doi:10.1002/2013JC009212, 2013.

Mercier, H., and Colin de Verdiere, A.: Space and time scales of mesoscale motions in the eastern North Atlantic, J. Phys. Oceanogr., 15, 171-183, 1985.

Mourino, B., Fernandez, E., Etienne, H., Hernandez, F., and Giraud, S.: Significance of cyclonic SubTropical Oceanic Rings of Magnitude (STORM) eddies for the carbon budget of the euphotic layer in the subtropical northeast Atlantic, J. Geophys. Res., 108 (C12), 3383, doi:10.1029/2003JC001884, 2003.

Navarro-Pérez, E., and Barton, E.D.: Seasonal and interannual variability of the Canary Current, Scientia Marina, 65(S1), 205-213, 2001.

New A.L., Jia, Y., Coulibaly, M., and Dengg, J.: On the role of the Azores current in the ventelation of the North Atlantic Ocean, *Progress in Oceanography*, **48**: 163-194, 2001.

Nolasco R., Cordeiro Pires, A., Cordeiro, N., Dubert, J.: A high-resolution modeling study of the Western Iberian Margin mean and seasonal upper ocean circulation, Ocean Dynamics, 63, 1041-1062, 2013.

Oliveira, P.B., Peliz, A., Dubert, J., Rosa, T.L., and Santos, A.M.P.: Winter geostrophic currents and eddies in the western Iberia coastal transition zone, Deep Sea Research I, 51(3), 367-381, 2004.

Onken, R.: The Azores Countercurrent, *Journal of Physical Oceanography*, 23, 1638-1646, 1993.

Owens, W.B., and Hogg, N.G.: Oceanic observations of stratified Taylor columns near a bump, Deep Sea Res., 27, 1029-1045, 1980.

Paillet, J., and Mercier, H.: An inverse model of the eastern North Atlantic general circulation and thermocline ventilation, Deep-Sea Research I, 44 (8), 1293-1328, 1997.

Pedlosky, J.: Geophysical fluid dynamics, 2nd ed., Springer, New York, 1-710, 1987.

Pedlosky, J.: *Ocean circulation theory*, 2nd ed., Springer, New York, 1-453, 1998.

Pelegri, J.L., Arístegui, J., Cana, L., González-Dávila, M., Hernández-Guerra, A., Hernández-León, S., Marrero-Díaz, A., Montero, M.F., Sangrà, P., and Santana-Casiano, M.: Coupling between the open ocean and the coastal upwelling region off northwest Africa: water recirculation and offshore pumping of organic matter, Journal of Marine Systems, 54, 3–37, 2005.

Perez, F.F., Mintrop, L., Llinas, O., Glez-Davila, M., Castro, C.G., Alvarez, M., Kortzinger, A.: Mixing analysis of nutrients, oxygen and inorganic carbon in the Canary Islands region, Journal of Marine Systems, 28, 183–201, 2001.

Pingree, R.D.: Ocean structure and climate (Eastern North Atlantic): in situ measurement and remote sensing (altimeter), *Journal of the Marine Biological Association of the UK*, 82, 681-707, 2002.

Pingree, R.D., Kou Y.H., and Garcia-Soto C.: Can Subtropical North Atlantic permanent thermocline be observed from space?, *Journal of the Marine Biological Association of the UK*, 82, 709-728, 2002.

Pingree, R.D., and Le Cann, B.: Anticyclonic eddy X91 in the southern Bay of Biscay, May 1991 to February 1992, J. Geophys. Res., 97, C9, 14353-14367, 1992.

Pingree, R.D., and Sinha, B.: Dynamic Topography (ERS-1/2 and sea truth) of subtropical ring (STORM 0 in the STORM Corridor (32-34oN), Eastern Basin, North Atlantic Ocean, *Journal of the Marine Biological Association of the UK*, 78, 351-376, 1998.

Pollard, R.T., and Pu, S.: Structure and Circulation of the upper Atlantic ocean Northeast of the Azores, *Progress in Oceanography*, 14, 443-462, 1985.

Pollard, R.T., Griffiths, M.J., Cunningham, S.A., Read, J.F., Perez, F.F., and Rios, A.F.: Vivaldi 1991- a study of the formation, circulation and ventilation of Eastern North Atlantic Central Water, *Progress in Oceanography*, 37, 167-192, 1996.

Read, J.F., Pollard, R.T., Miller, P.I., and Dale, A.C., 2010. Circulation and variability of the North Atlantic Current in the vicinity of the Mid-Atlantic Ridge. Deep-Sea Research I, 57, 307-318.

Reid, J.L.: On the middepth circulation and salinity field in the North Atlantic Ocean, J. Geophys. Res., 83(C10), 5063–5067, doi:10.1029/JC083iC10p05063, 1978.

Richardson, P.L., McCartney, P.L., Maillard, C.: A search for Meddies in historical data, Journal of Physical Oceanography, 15, 241-265, 1991.

Richardson, P.L., Bower, A.S., Zenk, W.: A census of meddies tracked by floats, Progress in Oceanography, 45 (2), 209-250, 2000.

Rio, M. H., Guinehut, S., Larnicol, G.: New CNES-CLS09 global mean dynamic topography computed from the combination of GRACE data, altimetry, and in situ measurements, Journal of Geophysical Research, 116(C7), doi: 10.1029/2010JC006505, 2011.

Roemmich, D., and Gilson, J.: The 2004–2008 mean and annual cycle of temperature, salinity, and steric height in the global ocean from the Argo Program, Progress in Oceanography, 82 (2), 81-100, 2009.

Schmidtko, S., Johnson, G.C., and Lyman, J.M.: MIMOC: A global monthly isopycnal upper-ocean climatology with mixed layers, Journal of Geophysical Research: Oceans, 118, 1658-1672, 2013.

Shoosmith, D.R., Richardson, P.L., Bower, A.S., and Rossby, H.T.: Discrete eddies in the northern North Atlantic as observed by looping RAFOS floats, Deep-Sea Research II, 52, 627–650, 2005.

Sparnocchia, S., Manzella, G.M., and La Violette, P.E.: The interannual and seasonal variability of the MAW and LIW core properties in the Western Mediterranean Sea. Coastal and Estuarine Studies, 46, 177-194, 1994.

Stammer, D.: Global Characteristics of Ocean Variability Estimated from Regional TOPEX/POSEIDON Altimeter Measurements, Journal of Physical Oceanography, 27, 1743–1769, 1997.

Troupin, C., Machín, F., Ouberdous, M., Sirjacobs, D., Barth, A., and Beckers, J.M.: High-resolution climatology of the northeast Atlantic using Data-Interpolating Variational Analysis (Diva), J. Geophys. Res., 115, C08005, doi:10.1029/2009JC005512, 2010.

Volkov, D. L., and Fu, L.L.: On the Reasons for the Formation and Variability of the Azores Current, J. Phys. Oceanogr., 40, 2197-2220, 2010.

WOA13, World Ocean Atlas 2013, available at http://www.nodc.noaa.gov/OC5/, temperature compiled by Locarnini, R. A., A.V. Mishonov, J.I. Antonov, T.P. Boyer, H.E. Garcia, O.K. Baranova, M.M. Zweng, C.R. Paver, J.R. Reagan, D.R. Johnson, M. Hamilton, D. Seidov, 2013. *World Ocean Atlas 2013, Volume 1: Temperature*. S. Levitus, Ed.; A. Mishonov, Technical Ed.; NOAA Atlas NESDIS 73, 40 pp., and salinity compiled by Zweng, M.M, J.R. Reagan, J.I. Antonov, R.A. Locarnini, A.V. Mishonov, T.P. Boyer, H.E. Garcia, O.K. Baranova, D.R. Johnson, D. Seidov, M.M. Biddle, 2013. *World Ocean Atlas 2013, Volume 2: Salinity*. S. Levitus, Ed.; A. Mishonov, Technical Ed.; NOAA Atlas NESDIS 74, 39 pp.

WOA09, World Ocean Atlas 2009, available at http://www.nodc.noaa.gov/OC5/WOA09/pubwoa09.html, temperature compiled by Locarnini, R.A., A.V. Mishonov, J.I. Antonov, T.P. Boyer, H.E. Garcia, O.K. Baranova, M.M. Zweng, and D.R. Johnson, 2010. *World Ocean Atlas 2009, Volume*

1: Temperature. S. Levitus, Ed. NOAA Atlas NESDIS 68, U.S. Government Printing Office, Washington, D.C., 184 pp., and salinity compiled by Antonov, J.I., D. Seidov, T.P. Boyer, R.A. Locarnini, A.V. Mishonov, H.E. Garcia, O.K. Baranova, M.M. Zweng, and D.R. Johnson, 2010. *World Ocean Atlas 2009, Volume 2: Salinity*. S. Levitus, Ed. NOAA Atlas NESDIS 69, U.S. Government Printing Office, Washington, D.C., 184 pp.

WOD, World Ocean Database. Boyer, T.P., J.I. Antonov, O.K. Baranova, C.Coleman, H.E. Garcia, A.Grodsky, D.R. Johnson, R.A. Locarnini, A.V. Mishonov, T.D. O'Brien, C.R. Paver, J.R. Reagan, D. Seidov, I.V. Smolyar, M.M. Zweng, 2013, World Ocean Database 2013. Sydney Levitus, Ed.; A. Mishonov, Technical Ed.; NOAA Atlas NESDIS 72, 209.

Figure captions

Fig.1. Scatter plot of valid temperature-salinity data-points (a) at 100 m, (b) 1900 m, (c) 2000 m and (d) the vertical profile of the number of valid temperature-salinity data points. WOA09 grid is shown on panels a-c with black dots. In plates (a-c) the colour scale represents salinity. In plate (d) black line with markers is total number of data points, grey line – PFL data only, red line – CTD data only, blue line – OSD data only.

Fig. 2. Weight function (W) (a) for small effect of topography at 100 m, (b) stronger effect at the same location at 1500 m and (c-d) the dominating effect of topography near the continental slope at 100 m. Lower panels show the shape of the weight function (c) when the correction factor w is not applied, and (d) with the correction factor w applied. The color scale marks the distribution of the weights as a function of the distance from the central grid-point (marked with the white ring). Topographic contours of 0, 500, 1000, 2000, 3000 and 4000 m are presented for reference.

Fig. 3. Radius (km) of the window containing a minimum of 30 data points: (a) at 100 m and (b) at 2500 m depth. Isolines of R = 100 km (solid), 200 km (dashed), 300 km (dash-dotted) and 400 km (dotted) are shown. (c) Variation of the window size as a function of the distance from the coast and water level. (d) Barnes' response function for different radii of averaging after the 3rd iteration.

Fig. 4 Spatial variation of R in (a) the upper 1900-m layer; (b) below 2000 m. Isolines of 100 km (magenta solid), 200 km (magenta dashed), 300 km (magenta dash-dotted) and 400 km (magenta dotted) are added. (c) presents total number of valid salinity data points at the selected neutral density surfaces. The numbers to the right of the black filled circles mark area-mean depth of the neutral density surface in the study region (not all numbers are presented).

Fig. 5. Vertical meridional sections of temperature along (a) 30°W and (b) 15°W; and zonal sections of salinity along (c) 31°N and (d) 38°N. The dashed isolines show positions of neutral density surfaces (only part of the surfaces used are shown).

Fig. 6. Vertical meridional sections of temperature along 17°W (a) - MEDTRANS, (b) – WOA13, (c) – MIMOC, (d) - MEDTRANS minus WOA13, (e) – MEDTRANS minus MIMOC.

Fig. 7. Temperature at 600 m. (a) and (g) - MEDTRANS, (b) – WOA09, (c) - MEDTRANS minus WOA09, (d) and (e) – MIMOC, (f) – MEDTRANS minus MIMOC, (h) – WOA13, (i) - MEDTRANS minus WOA13.

Fig. 8. Salinity at 1200 m. (a) and (g) - MEDTRANS, (b) – WOA09, (c) - MEDTRANS minus WOA09, (d) and (e) – MIMOC, (f) – MEDTRANS minus MIMOC, (h) – WOA13, (i) - MEDTRANS minus WOA13

Fig. 9. Salinity at 1700 m. (a) and (g)- MEDTRANS, (b) – WOA09, (c) - MEDTRANS minus WOA09, (e) – MIMOC, (f) – MEDTRANS minus MIMOC, (h) – WOA13, (i) - MEDTRANS minus WOA13. On plate (d) are presented vertical profiles of MEDTRANS (red) and MIMOC (blue) at the points: 1(32N, 34W), 2 (40N, 34W), 3 (40N, 17W), 4 (37N, 8W). WOA13 profiles (black) are not seen since they are identical to MEDTRANS profiles for points 1-3 and to MIMOC profile for point 4. Dashed line over climatic profiles 3 are the observed CTD casts within 10-km distance from this point.

Fig. 10. N^2 mean (a) – (c) from 200 to 800 m, (d) – (f) from 700 to 1300 m, and (g) – (i) from 1400-2000 m, for MEDTRANS (the first column), WOA13 (the second column) and MIMOC (the third column).

Fig. 11. Velocity of geostrophic currents (cm s^{-1}) at 100 m referenced to 1900 m, derived from (a) MEDTRANS, (c) WOA13 and (d) MIMOC climatologies. AVISO surface currents, averaged between 1992 and 2012, are presented in (b). Velocity of geostrophic currents at 1000 m referenced to 1900 m (cm s^{-1}), derived from (e) MEDTRANS climatology and (f) WOA13. For reference, 2000 m and 3000 m depth contours are shown in white.

Fig. 12. Salinity at (a-b) 200 m, (d-e) 1100 m and (g-h) 1600 m: (a), (d) and (g) – winter; (b), (e) and (h) – summer; (c), (f) and (i) – difference between summer and winter climatologies.

Fig. 13. Velocity of geostrophic currents (cm s^{-1}) at 100 m and 700 m levels, referenced to 1900 m: (a) 100 m winter, (b) 100 m summer, (c) 700 m winter, (d) 700 m summer.

Fig. 14. (a) Positions of the axis of the lower MW core derived from MEDTRANS data-set (black dots), overlaid on bathymetry of the Iberian-Canary basins. (b) Seasonal variations of the depth and salinity of the lower MW core along the Iberian slope in winter (disks) and summer (squares). The vertical segments represent the maximum depth limits of $S \geq 0.99 * Smax$ at the section.

Fig. A1 (4) Regional-mean decorrelation scales (radii): black curve is the mean autocorrelation function, black diamond is the mean of the decorrelation scales, while black disk is the decorrelation scale computed from the mean autocorrelation function (black curve). Dash lines mark the level of significance of the mean autocorrelation function. Bars present the normalised histogram of regional-mean eddy radii.

Tables

Table 1. Profiles statistics per instrument type for 25-m vertically binned profiles. Percent good is calculated for both temperature and salinity

data type	number of profiles	>50% good	>75% good	>90% good
CTD	9973	99%	98%	96%
PFL	21634	96%	96%	95%
OSD	22822	96%	95%	91%
total	54429	97%	96%	93%

fig. 1

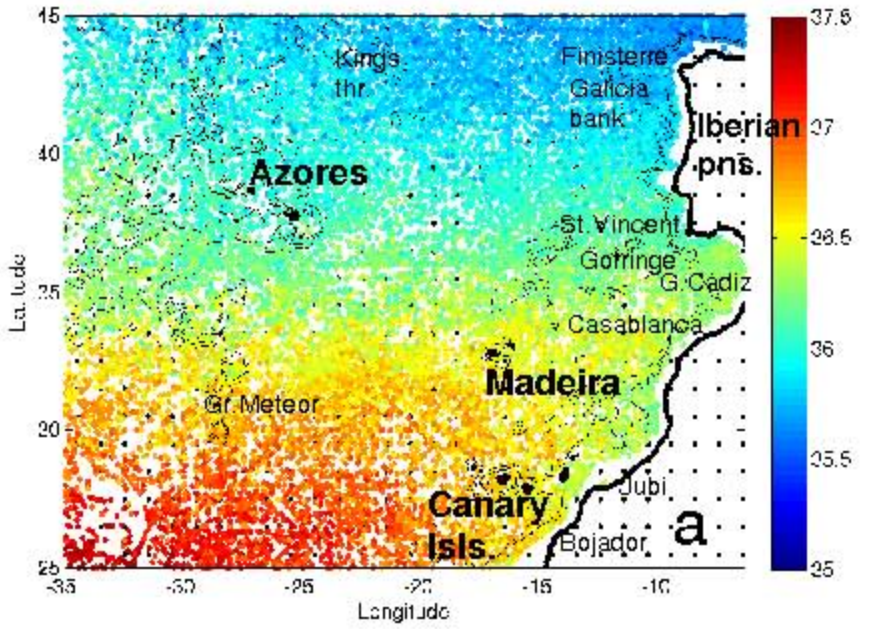
Kings thr.
Finisterre Galicia bank
Iberian pns.
Azores
St. Vincent
Gorringe
G. Cadiz
Casablanca
Madeira
Gr. Meteor
Canary Isls.
Jubi
Bojador
a
Latitude
Longitude

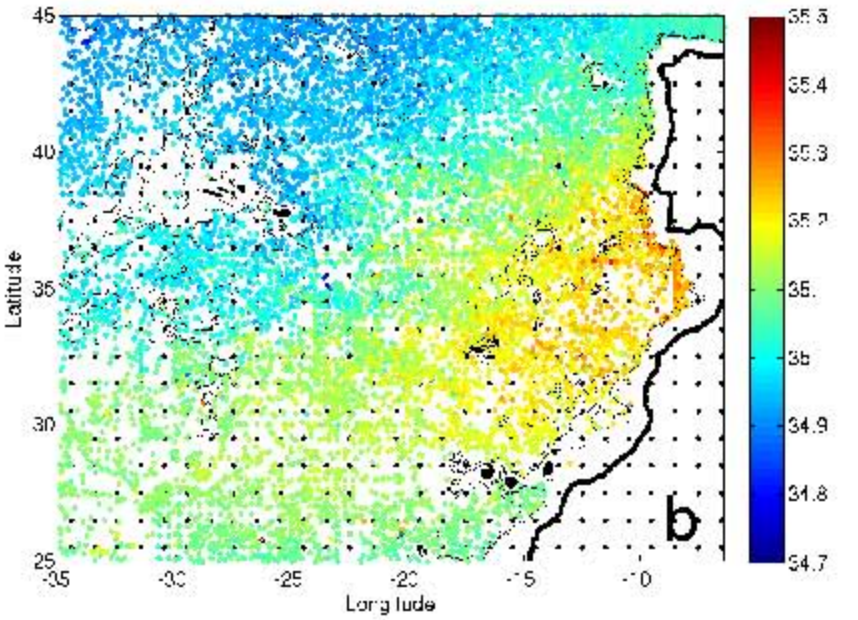
b
Latitude
Longitude

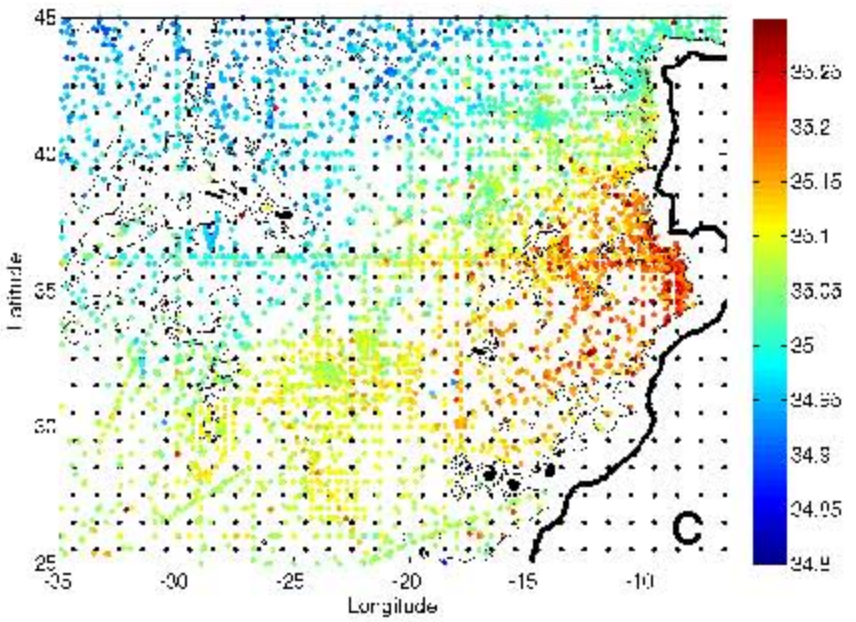
c
Latitude
Longitude

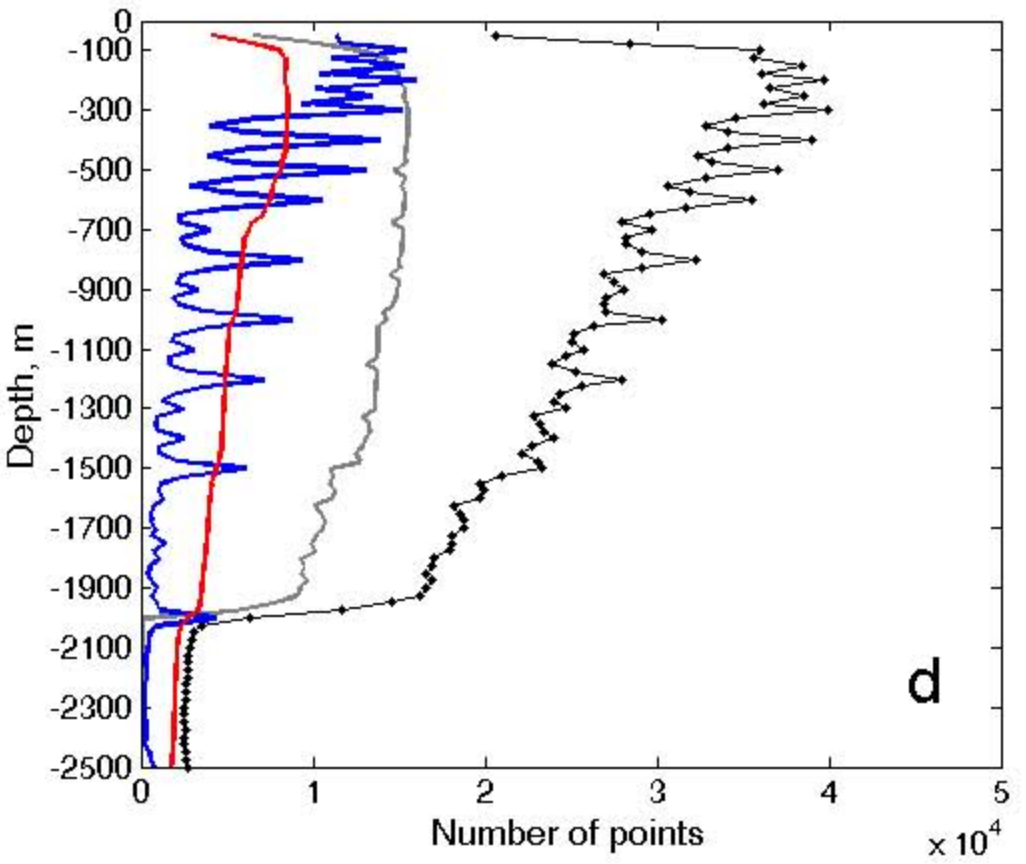
Depth, m
Number of points
x 10^4
d

fig. 2

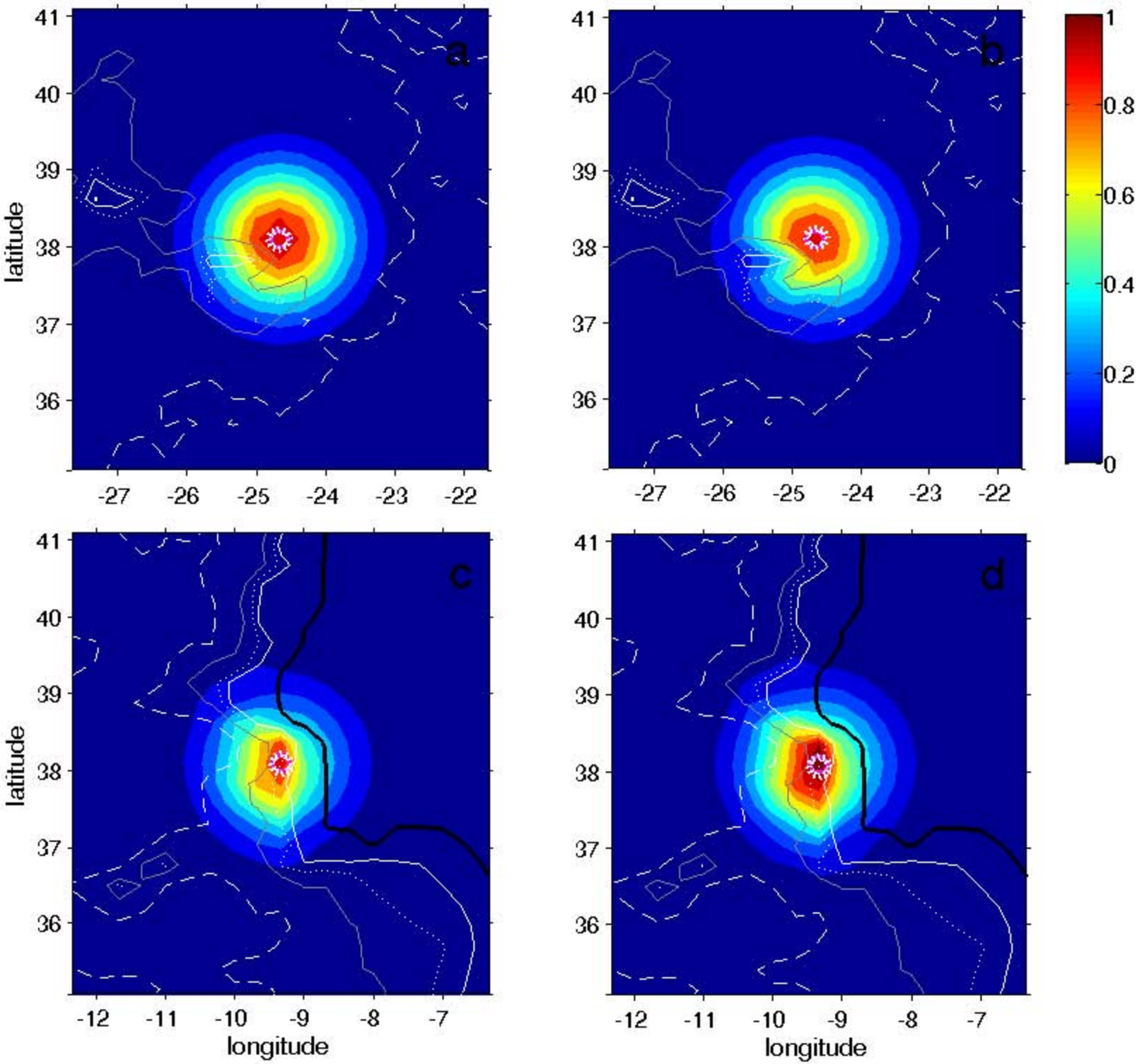
a
b
c
d
latitude
longitude
41
40
39
38
37
36
-27
-26
-25
-24
-23
-22
-12
-11
-10
-9
-8
-7
1
0.8
0.6
0.4
0.2
0

fig. 3

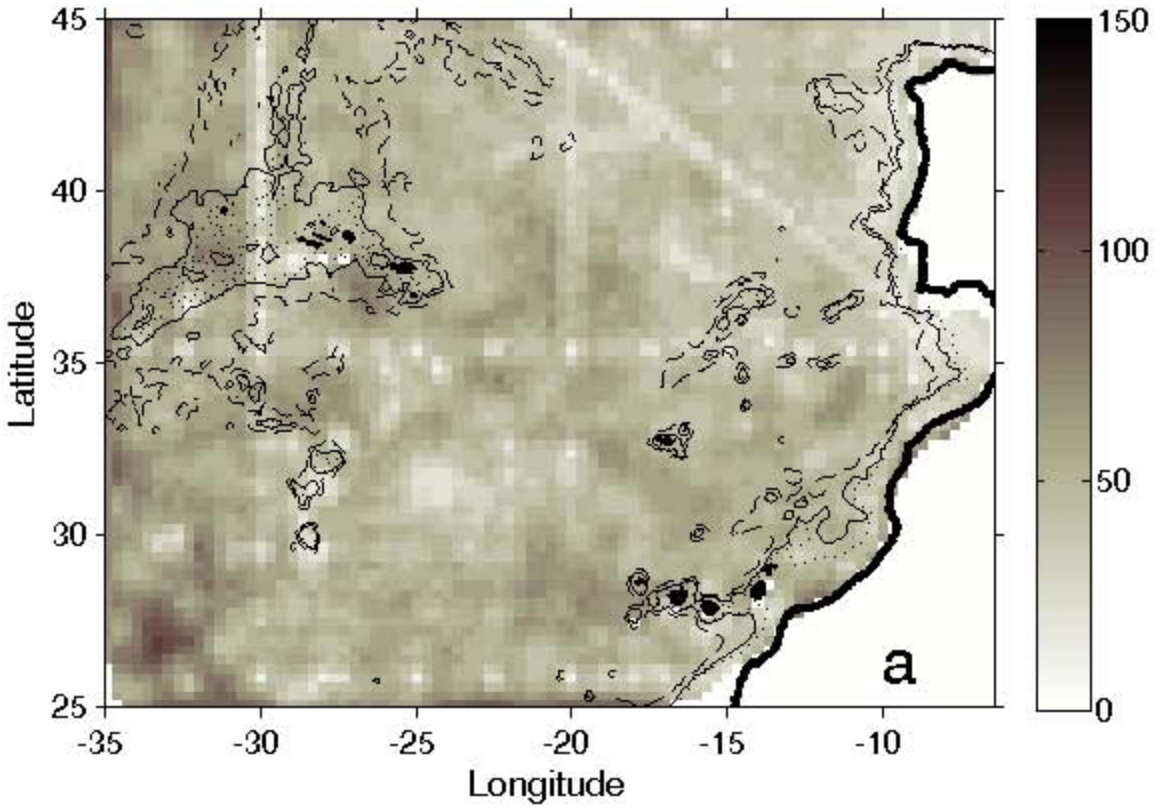
45
40
35
30
25
Latitude
-35
-30
-25
-20
-15
-10
Longitude
a
150
100
50
0

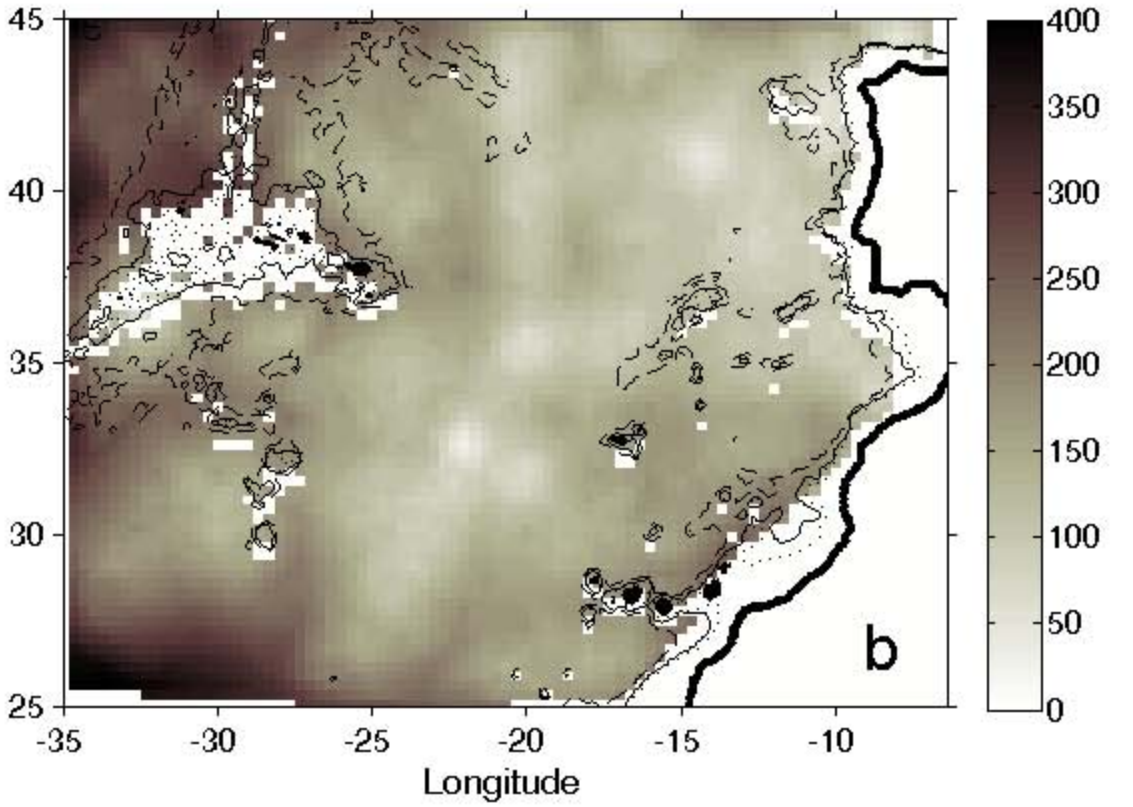
45
40
35
30
25
-35
-30
-25
-20
-15
-10
Longitude
b
400
350
300
250
200
150
100
50
0

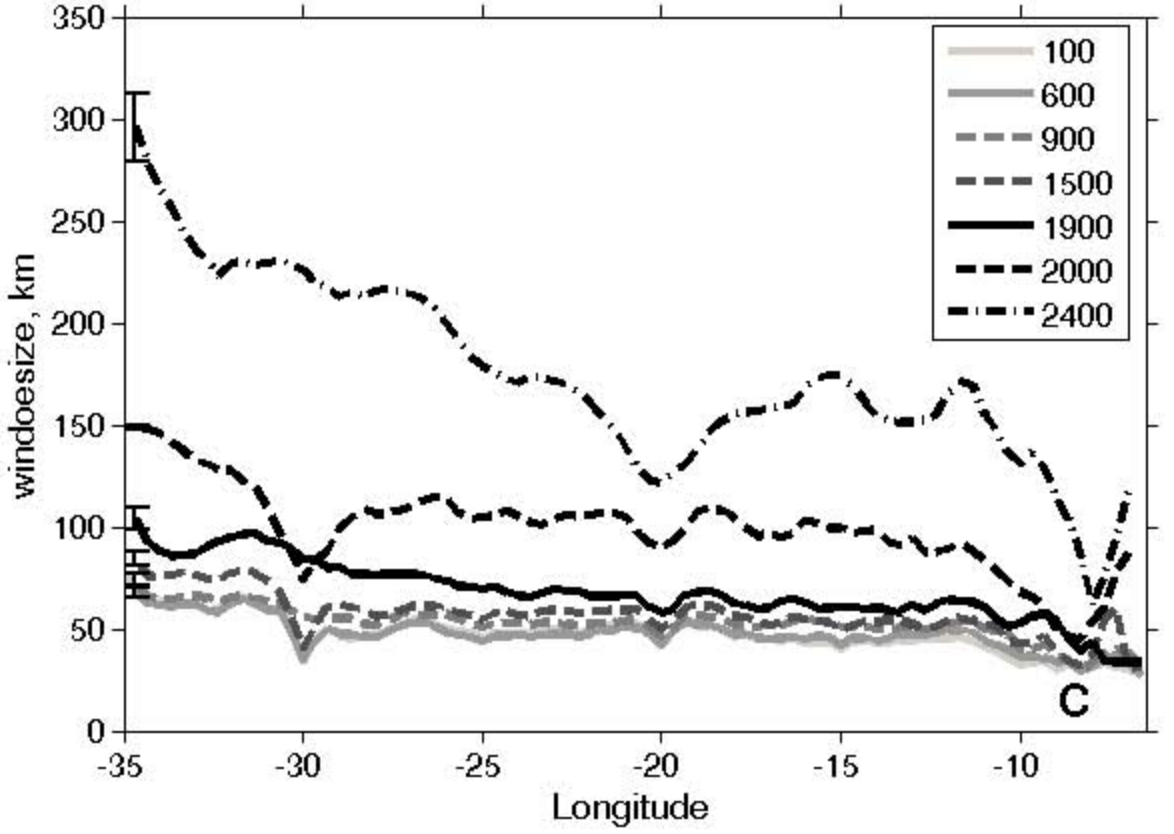
windoesize, km
350
300
250
200
150
100
50
0
-35
-30
-25
-20
-15
-10
Longitude
100
600
900
1500
1900
2000
2400
c

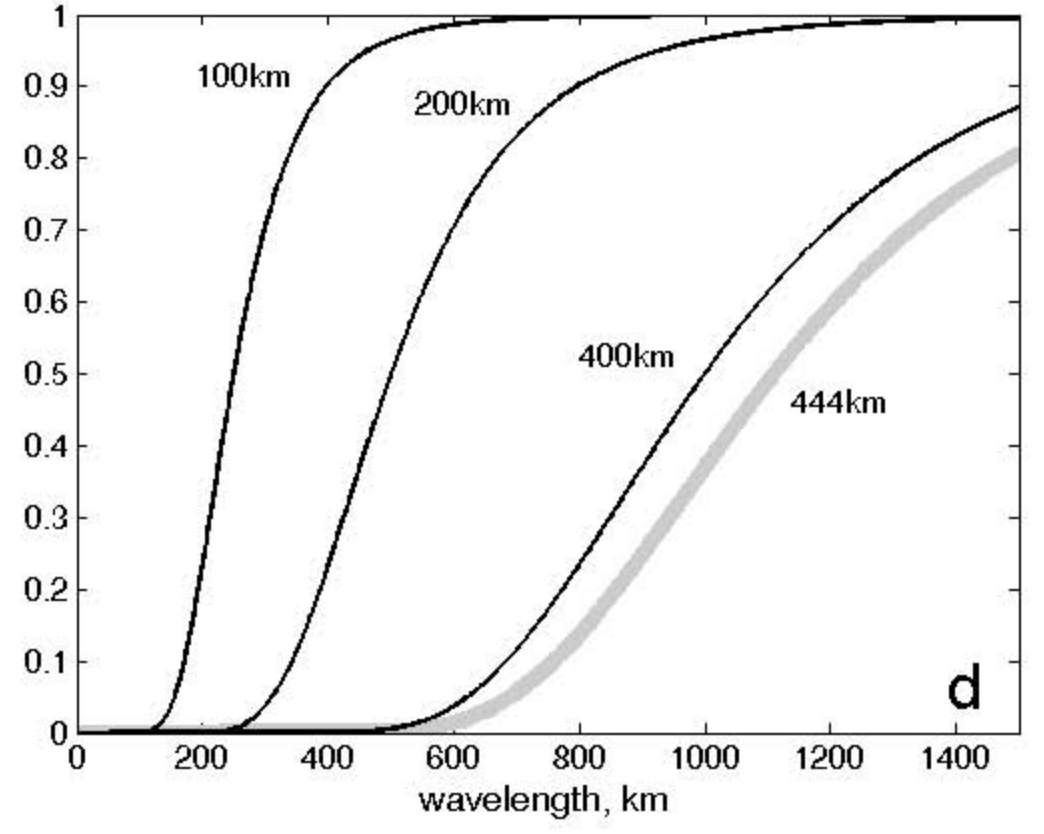
1
0.9
0.8
0.7
0.6
0.5
0.4
0.3
0.2
0.1
0
0
200
400
600
800
1000
1200
1400
wavelength, km
100km
200km
400km
444km
d

fig. 4

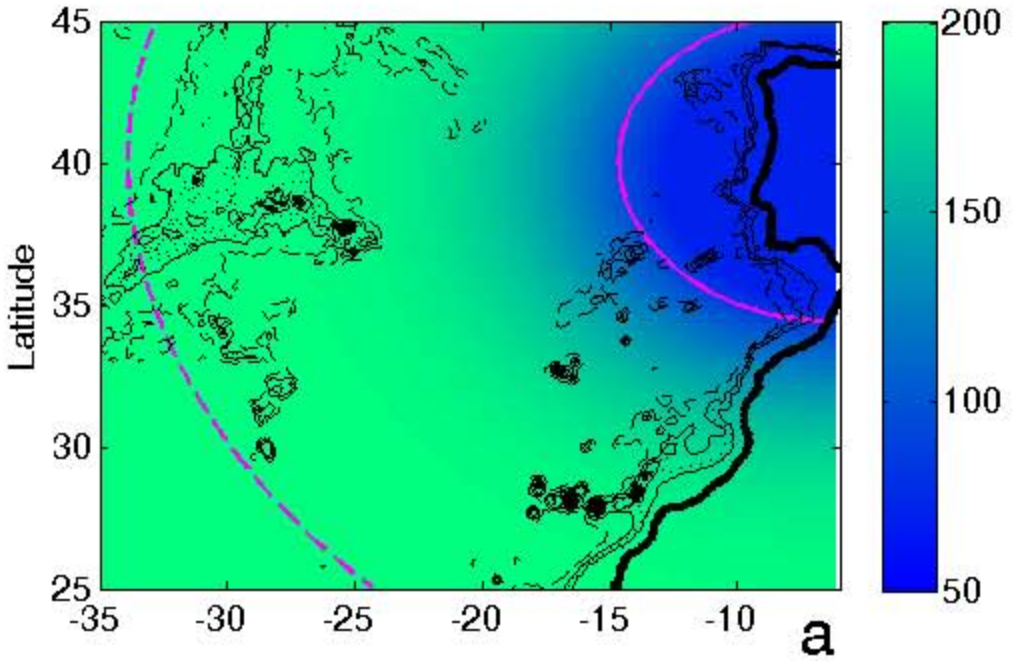
45
40
35
30
25
Latitude
-35
-30
-25
-20
-15
-10
a
200
150
100
50

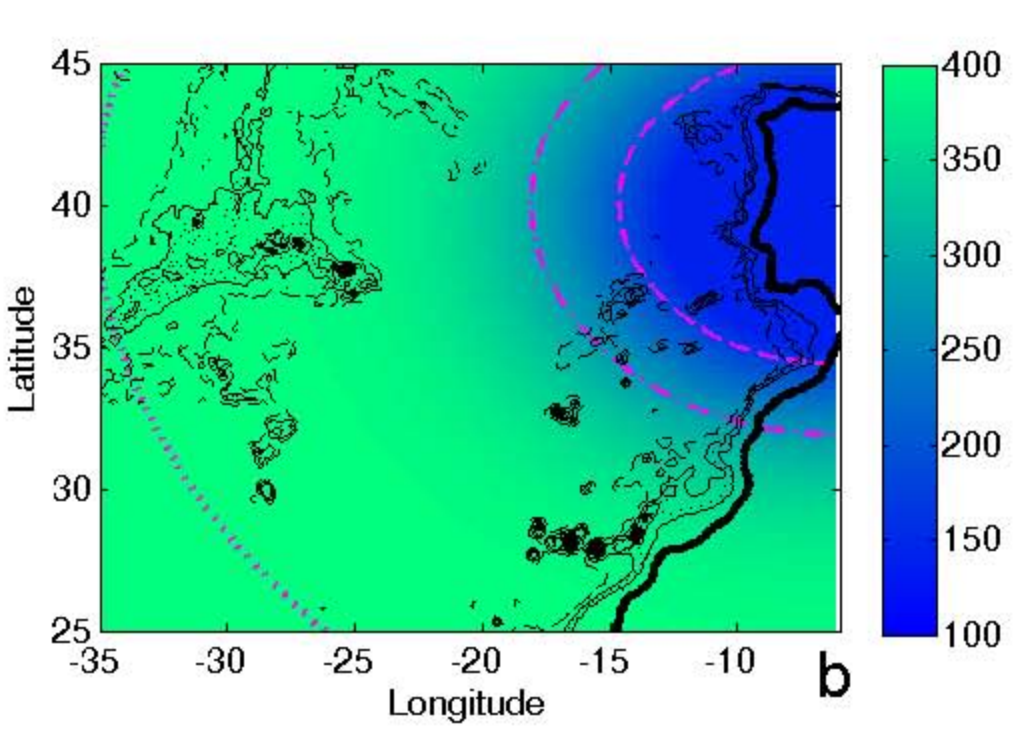
45
40
35
30
25
Latitude
-35
-30
-25
-20
-15
-10
Longitude
b
400
350
300
250
200
150
100

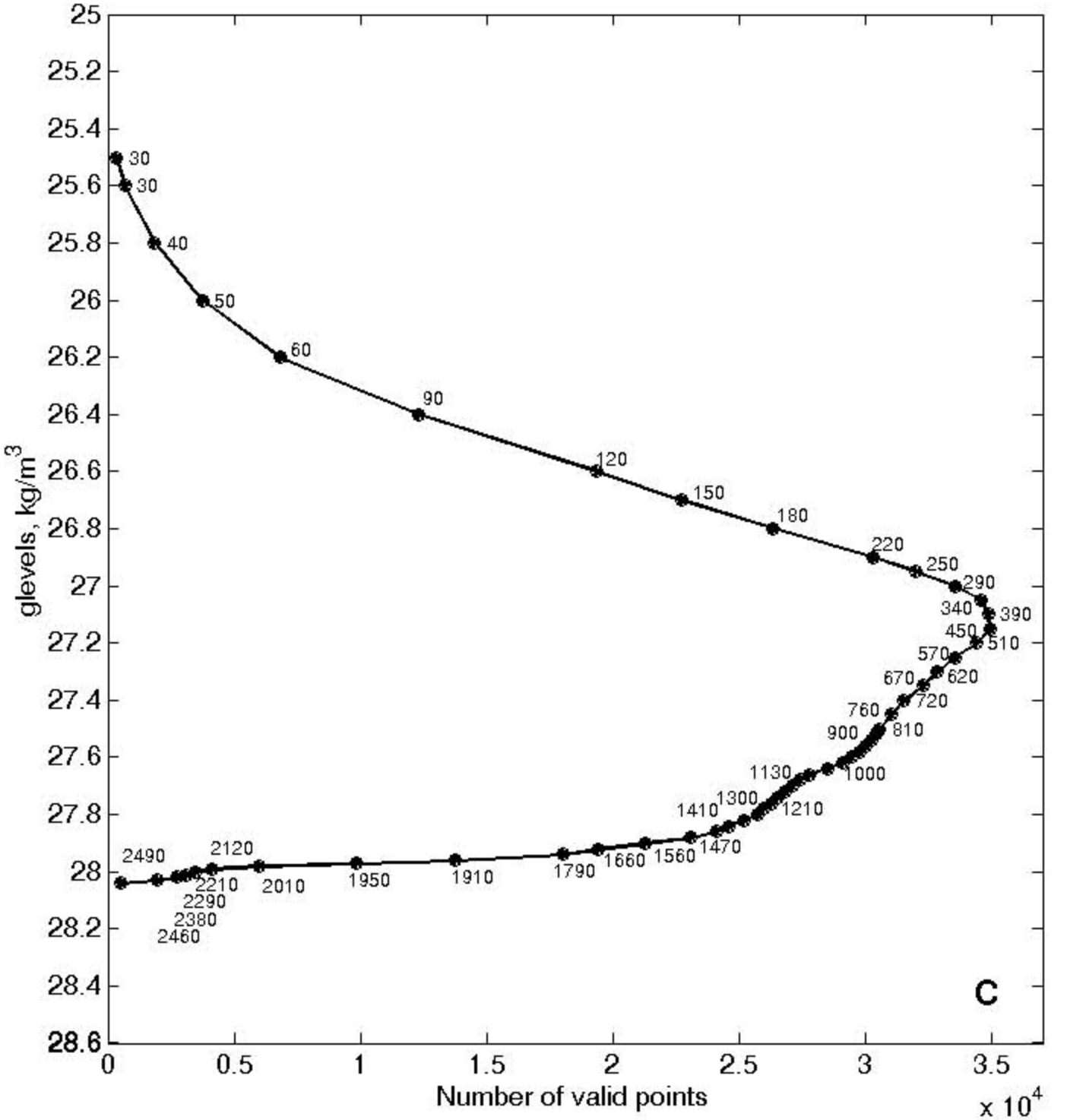
glevels, kg/m3
25
25.2
25.4
25.6
25.8
26
26.2
26.4
26.6
26.8
27
27.2
27.4
27.6
27.8
28
28.2
28.4
28.6
0
0.5
1
1.5
2
2.5
3
3.5
x 10^4
Number of valid points
c
30
30
40
50
60
90
120
150
180
220
250
290
340
390
450
510
570
620
670
720
760
810
900
1000
1130
1210
1300
1410
1470
1560
1660
1790
1910
1950
2010
2120
2210
2290
2380
2460
2490

fig. 5

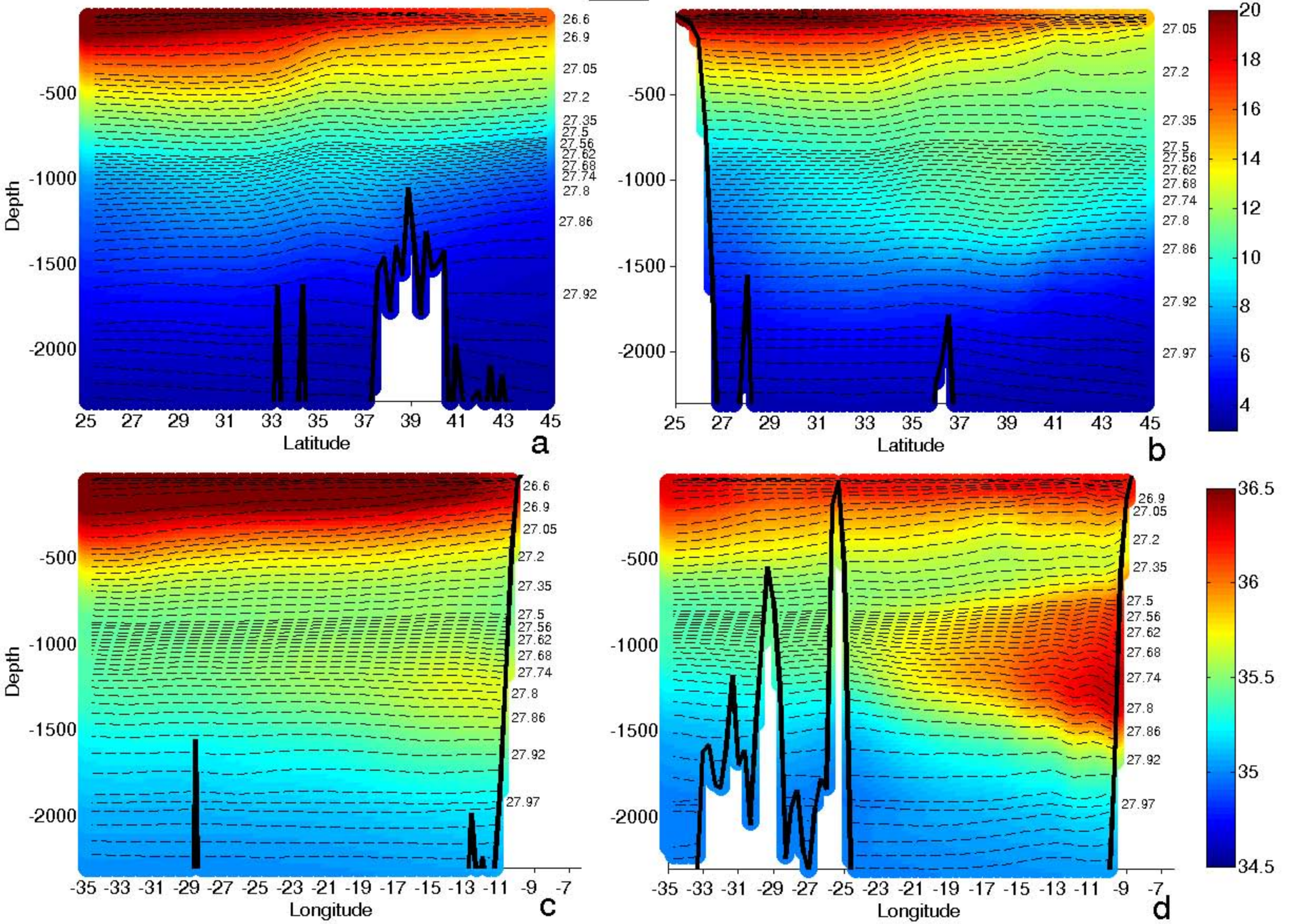
Depth
-500
-1000
-1500
-2000
25 27 29 31 33 35 37 39 41 43 45
Latitude
a
26.6
26.9
27.05
27.2
27.35
27.5
27.56
27.62
27.68
27.74
27.8
27.86
27.92
b
27.97
20
18
16
14
12
10
8
6
4
-35 -33 -31 -29 -27 -25 -23 -21 -19 -17 -15 -13 -11 -9 -7
Longitude
c
d
36.5
36
35.5
35
34.5

fig. 6

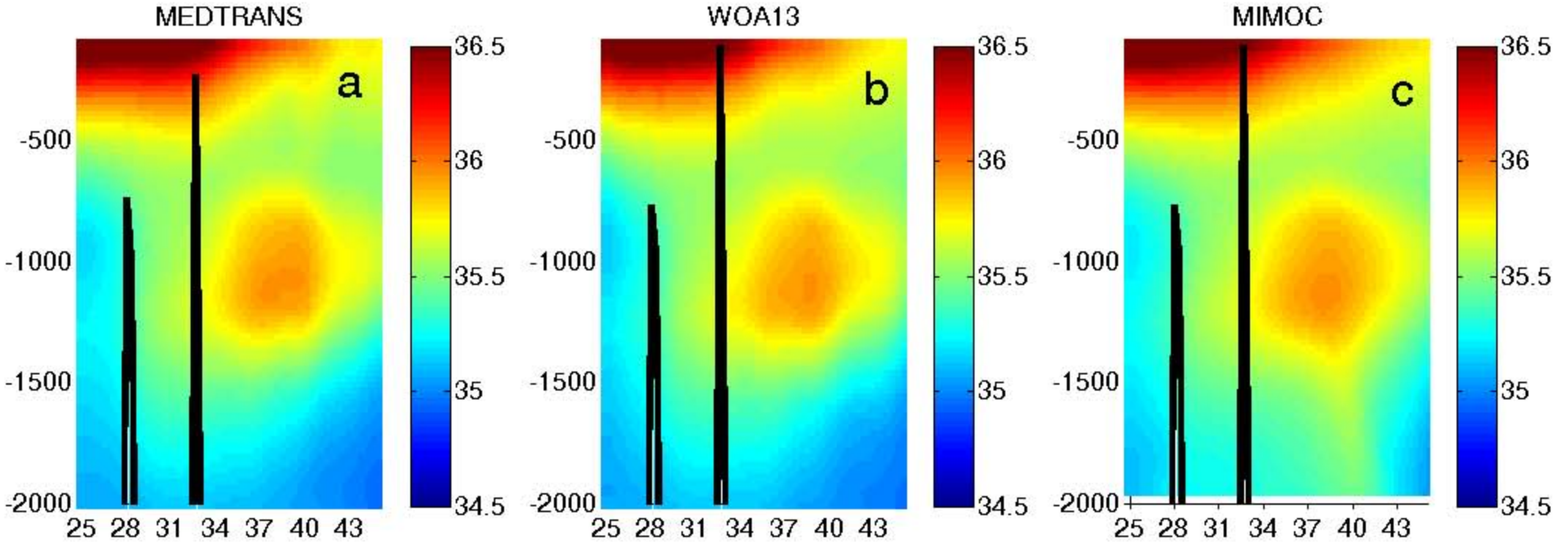
MEDTRANS
WOA13
MIMOC
a
b
c
-500
-1000
-1500
-2000
25 28 31 34 37 40 43
36.5
36
35.5
35
34.5
MEDTRANS-WOA13
MEDTRANS-MIMOC
d
e
0.05
0
-0.05
-0.1
-0.15
-0.2
-0.25

fig. 7

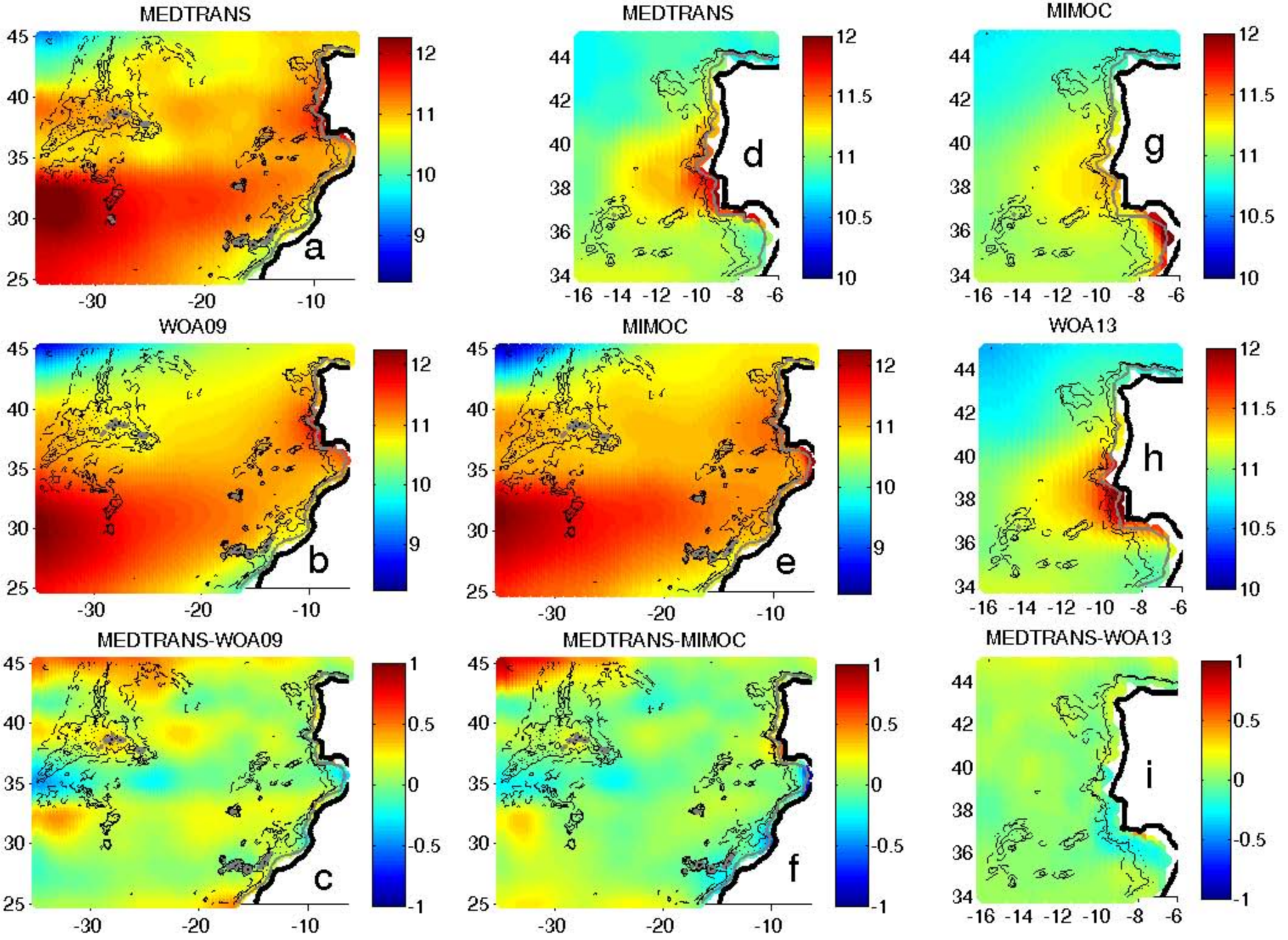
MEDTRANS
a
MEDTRANS
d
MIMOC
g
WOA09
b
MIMOC
e
WOA13
h
MEDTRANS-WOA09
c
MEDTRANS-MIMOC
f
MEDTRANS-WOA13
i

fig. 8

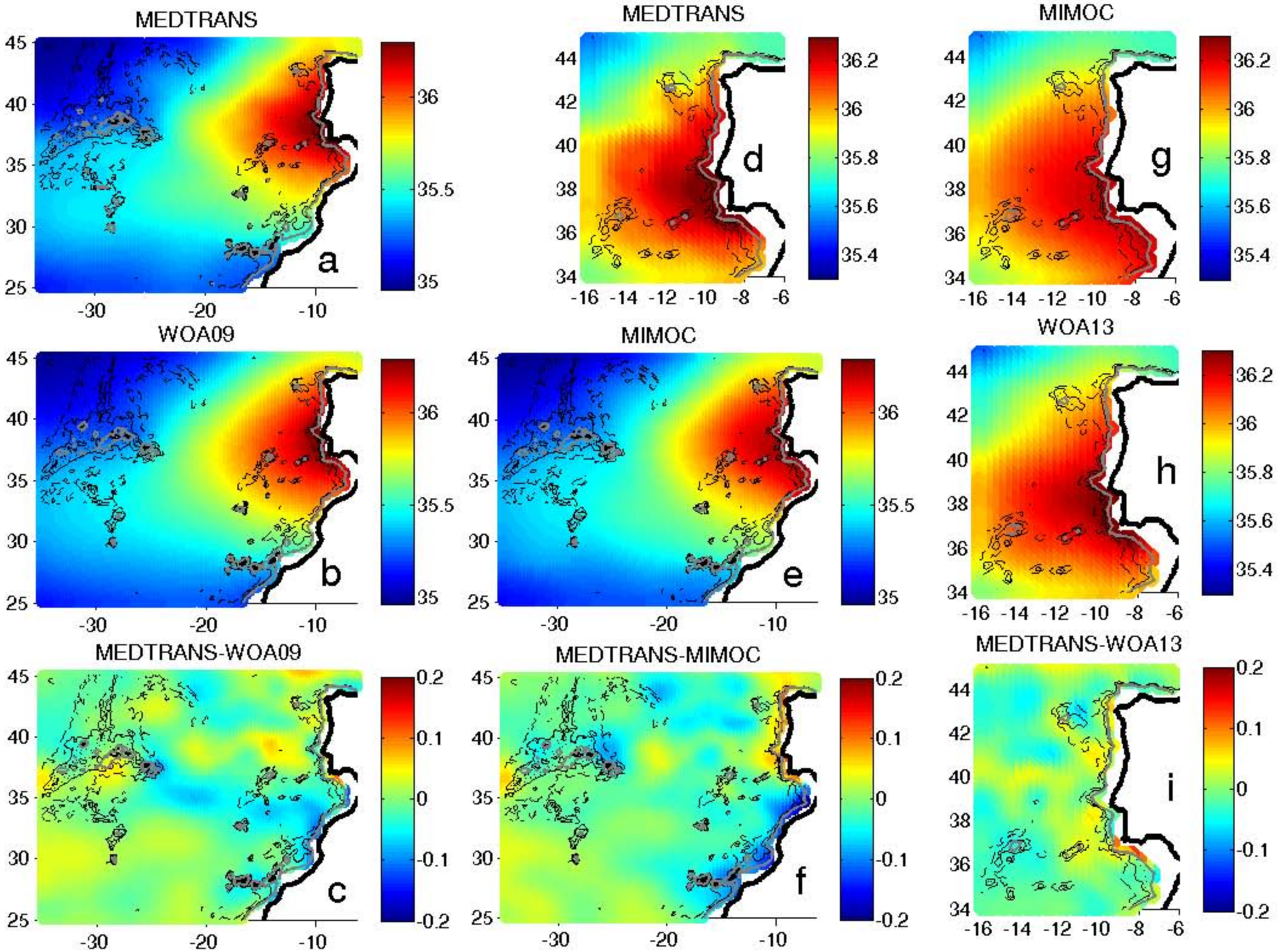
MEDTRANS
a
MEDTRANS
d
MIMOC
g
WOA09
b
MIMOC
e
WOA13
h
MEDTRANS-WOA09
c
MEDTRANS-MIMOC
f
MEDTRANS-WOA13
i

fig. 9

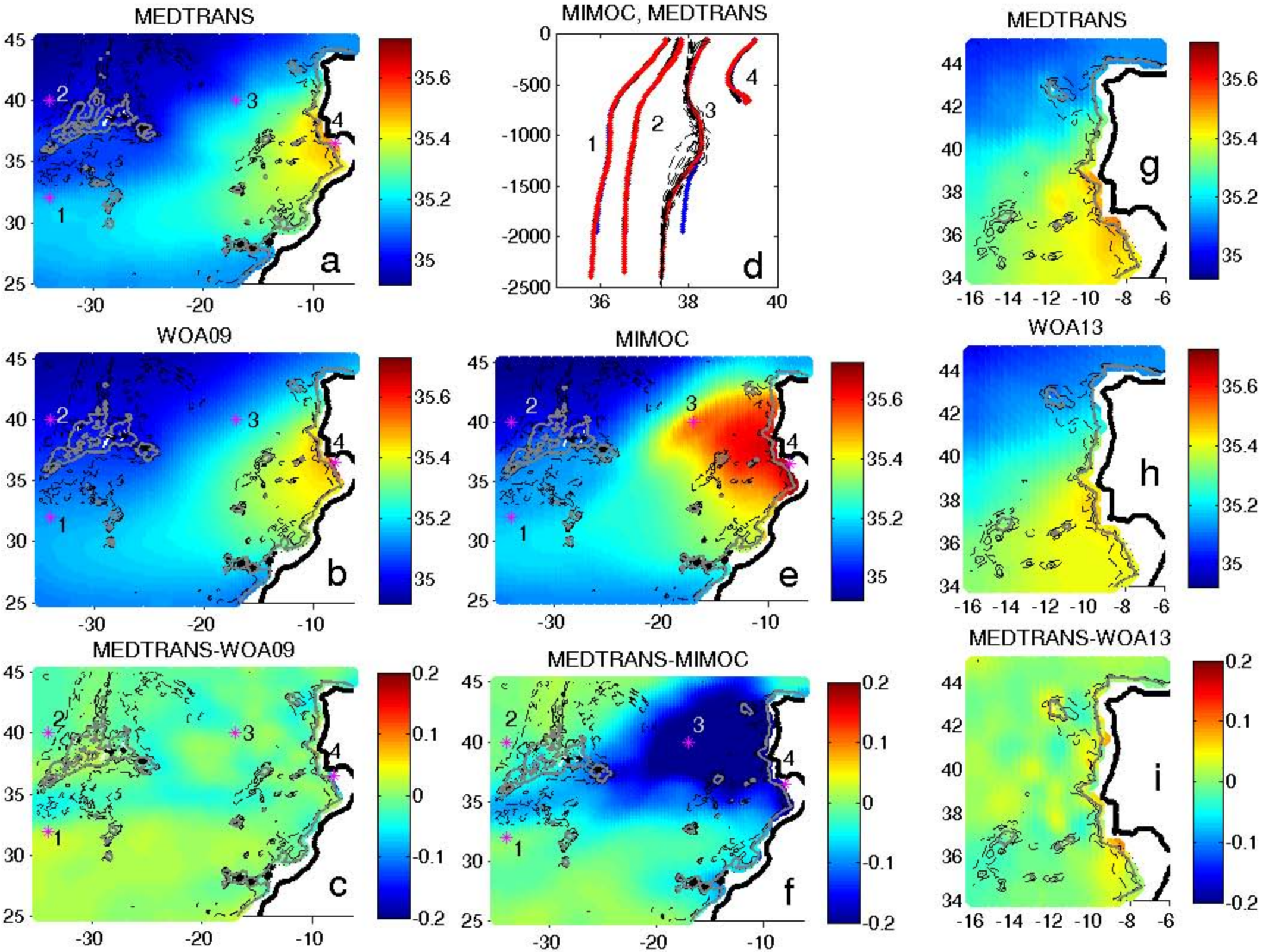
MEDTRANS
MIMOC, MEDTRANS
MEDTRANS
WOA09
MIMOC
WOA13
MEDTRANS-WOA09
MEDTRANS-MIMOC
MEDTRANS-WOA13
a
b
c
d
e
f
g
h
i
1
2
3
4
35.6
35.4
35.2
35
0.2
0.1
0
-0.1
-0.2

fig. 10

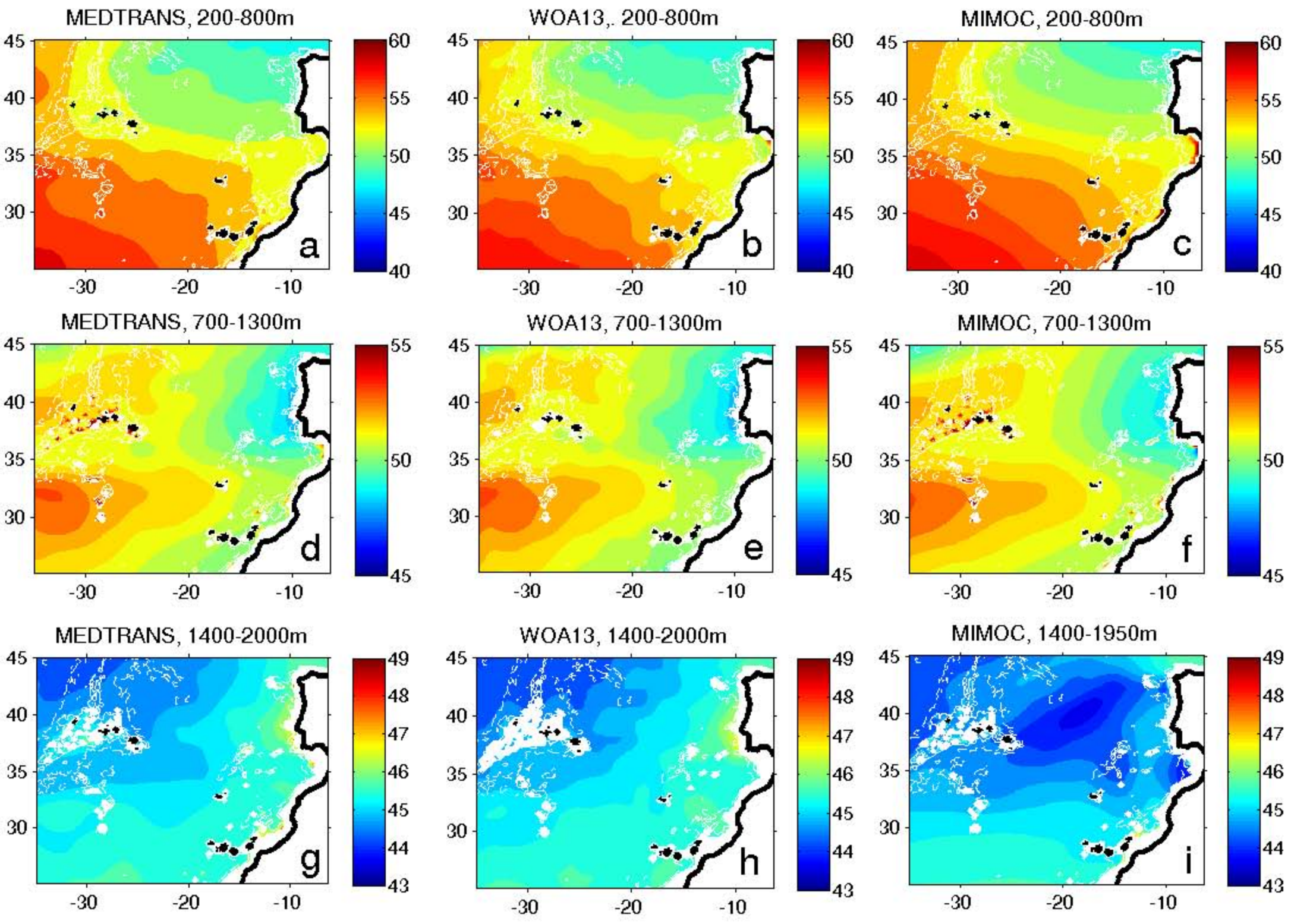
MEDTRANS, 200-800m
WOA13,. 200-800m
MIMOC, 200-800m
MEDTRANS, 700-1300m
WOA13, 700-1300m
MIMOC, 700-1300m
MEDTRANS, 1400-2000m
WOA13, 1400-2000m
MIMOC, 1400-1950m
a
b
c
d
e
f
g
h
i
45
40
35
30
-30
-20
-10
60
55
50
45
40
49
48
47
46
44
43

fig. 11

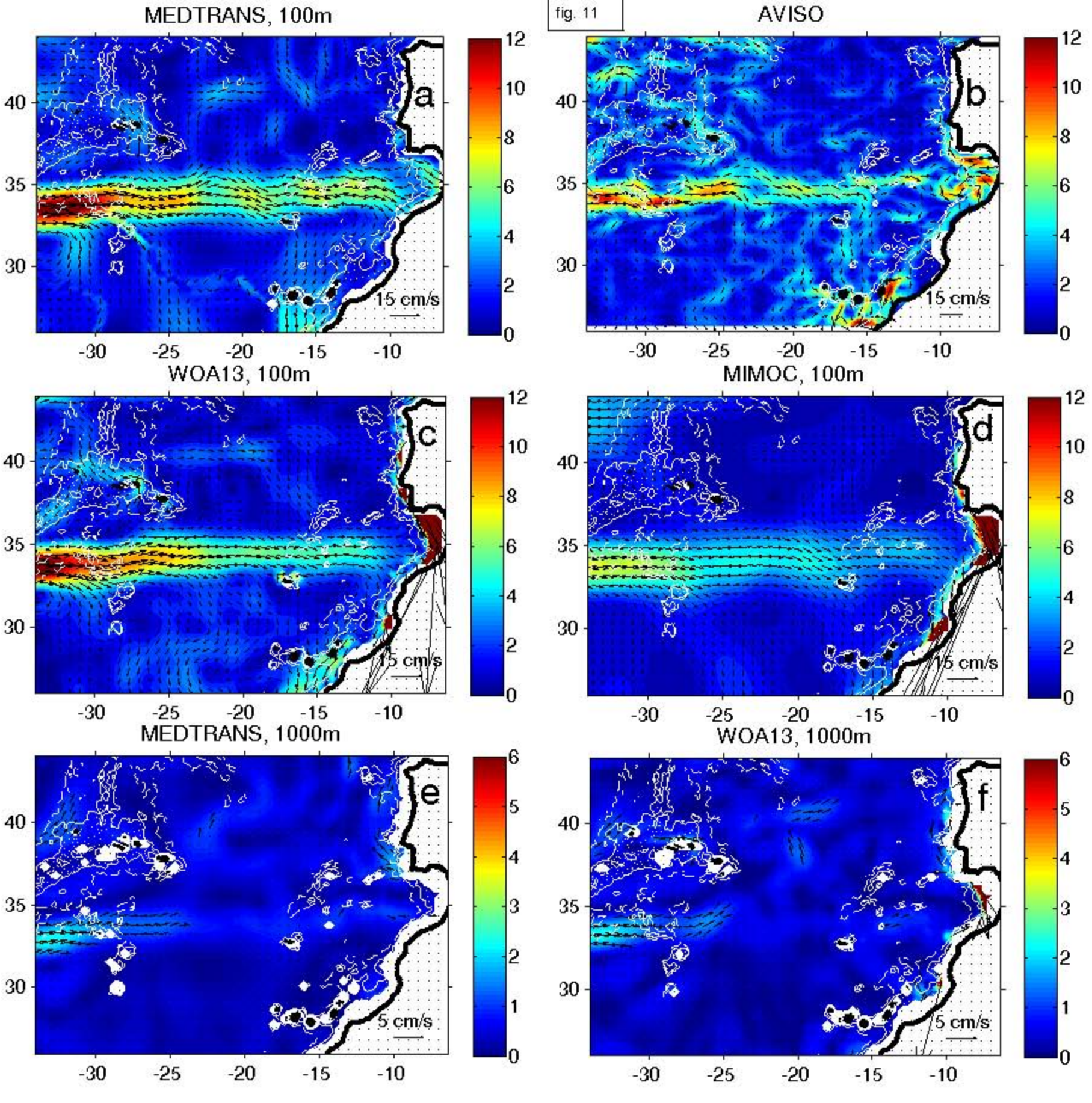
MEDTRANS, 100m
AVISO
WOA13, 100m
MIMOC, 100m
MEDTRANS, 1000m
WOA13, 1000m
a
b
c
d
e
f
15 cm/s
5 cm/s
40
35
30
-30
-25
-20
-15
-10
0
2
4
6
8
10
12
1
3
5

fig. 12

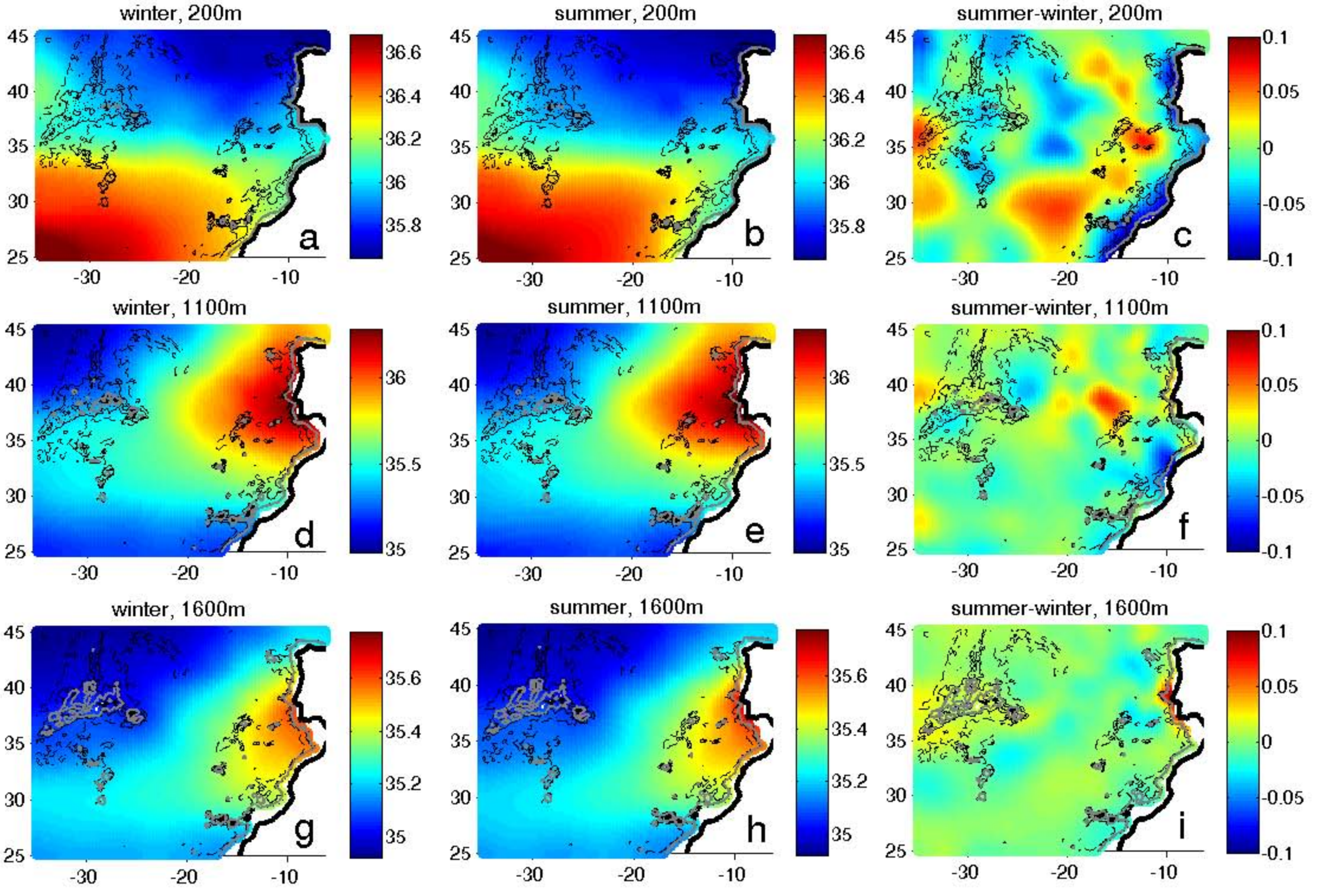
winter, 200m
summer, 200m
summer-winter, 200m
winter, 1100m
summer, 1100m
summer-winter, 1100m
winter, 1600m
summer, 1600m
summer-winter, 1600m
a
b
c
d
e
f
g
h
i
45
40
35
30
25
-30
-20
-10
36.6
36.4
36.2
36
35.8
35.5
35
35.6
35.4
35.2
0.1
0.05
0
-0.05
-0.1

fig. 13

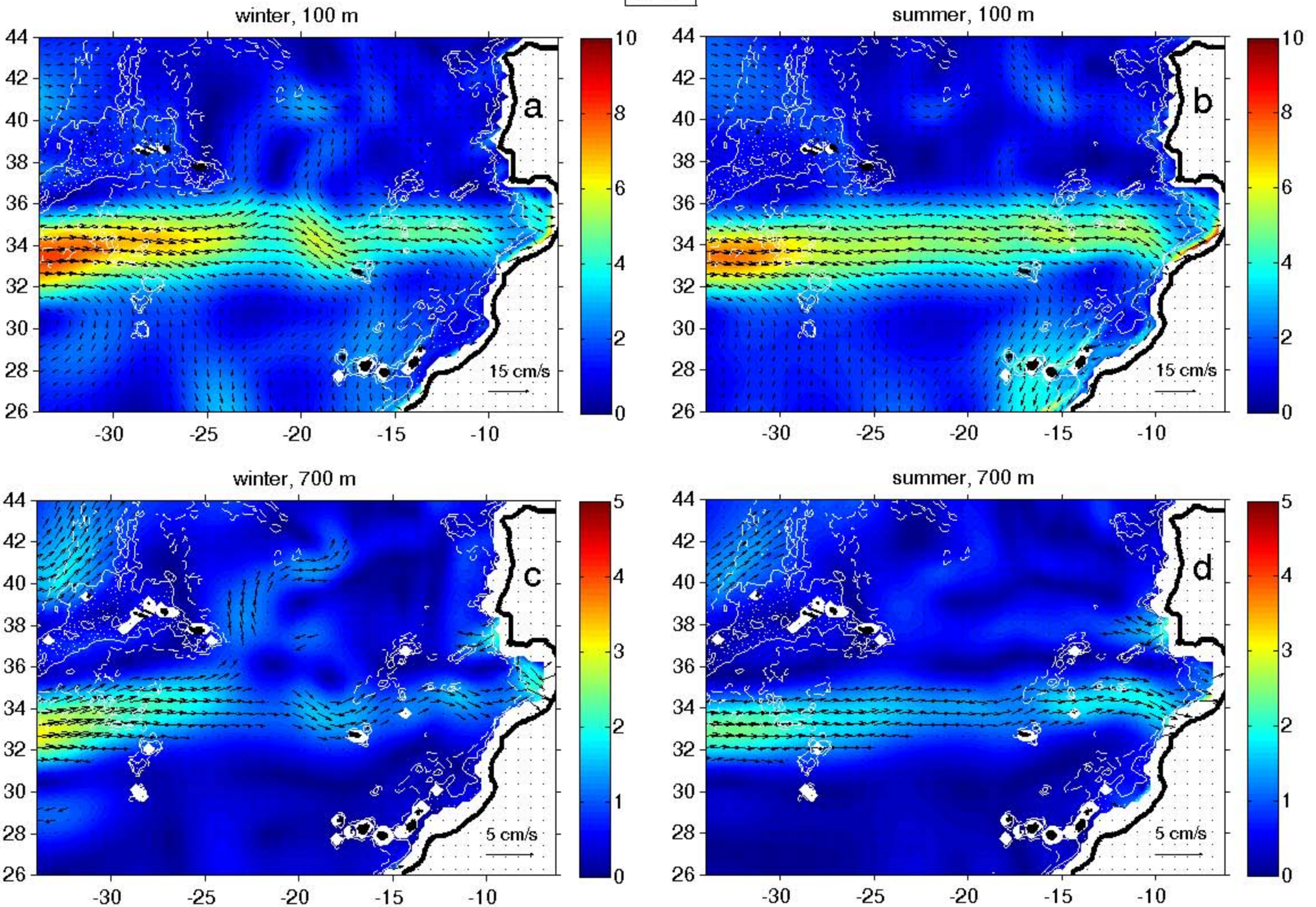
winter, 100 m
summer, 100 m
winter, 700 m
summer, 700 m
a
b
c
d
15 cm/s
5 cm/s
44
42
40
38
36
34
32
30
28
26
-30
-25
-20
-15
-10
10
8
6
4
2
0
5
4
3
2
1
0

fig. 14

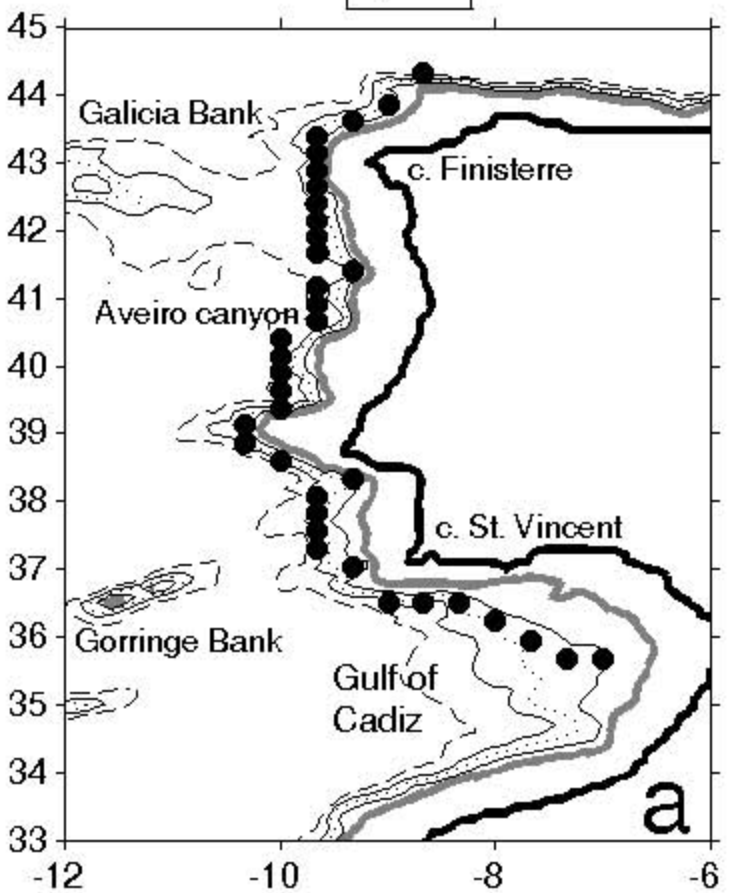
45
44
43
42
41
40
39
38
37
36
35
34
33
Galicia Bank
c. Finisterre
Aveiro canyon
c. St. Vincent
Gorringe Bank
Gulf of
Cadiz
a

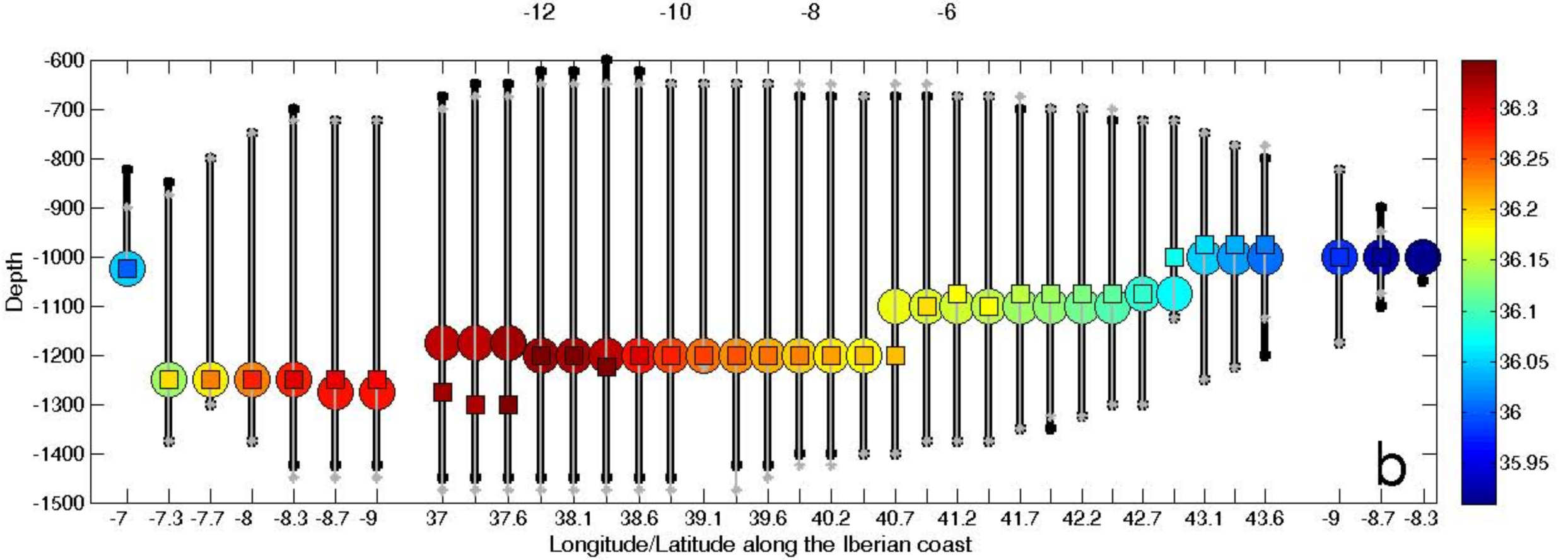
-12
-10
-8
-6
-600
-700
-800
-900
-1000
-1100
-1200
-1300
-1400
-1500
Depth
-7
-7.3
-7.7
-8
-8.3
-8.7
-9
37
37.6
38.1
38.6
39.1
39.6
40.2
40.7
41.2
41.7
42.2
42.7
43.1
43.6
-9
-8.7
-8.3
Longitude/Latitude along the Iberian coast
36.3
36.25
36.2
36.15
36.1
36.05
36
35.95
b

fig. A1